

Patterns, drivers, and ecological implications of upwelling in coral reef habitats of the southern Red Sea

Thomas M. DeCarlo^{1*}, Susana Carvalho¹, Laura Gajdzik¹, Royale S. Hardenstine¹, Lyndsey K. Tanabe¹, Rodrigo Villalobos¹, and Michael L. Berumen¹

¹Red Sea Research Center, Division of Biological and Environmental Science and Engineering, King Abdullah University of Science and Technology (KAUST), Thuwal, Saudi Arabia

*corresponding author: thomas.decarlo@kaust.edu.sa

Key Points:

- In the southern Red Sea, wind-driven upwelling in coral reef habitats is regulated by remote forcing from the southwest Indian Monsoon
- The skill of capturing the spatial and temporal patterns of upwelling varies among satellite-based sea surface temperature products
- Upwelling dampens southern Red Sea maximum temperatures by 1-3 °C, with important consequences for corals, sea turtles, and biodiversity

In prep for *Journal of Geophysical Research – Oceans*

Abstract

Coral reef ecosystems are highly sensitive to thermal anomalies, making them vulnerable to ongoing global warming. Yet, a variety of cooling mechanisms, such as upwelling, offer some respite to certain reefs. The Farasan Banks in the southern Red Sea is home to hundreds of coral reefs covering 16,000 km² and experiences among the highest water temperatures of any coral-reef region despite exposure to summertime upwelling. We deployed an array of temperature loggers on coral reefs in the Farasan Banks, enabling us to evaluate the skill of satellite-based sea surface temperature (SST) products for capturing patterns of upwelling. Additionally, we used remote sensing products to investigate the physical drivers of upwelling, and to better understand how upwelling modulates summertime heat stress on coral communities. Our results show that various satellite SST products underestimate reef-water temperatures but differ in their ability to capture the spatial and temporal dynamics of upwelling. Monsoon winds from June to September drive the upwelling in the southern Red Sea via Ekman transport of surface waters off the shelf, and this process is ultimately controlled by the southwest Indian monsoon in the Arabian Sea. Further, the timing of the cessation of monsoon winds regulates the maximum water temperatures that are reached in September and October. In addition to describing the patterns and mechanisms of upwelling, our study sheds light on the broad ecological implications of this upwelling system, including modulation of coral bleaching events and effects on biodiversity, sea turtle reproduction, fish pelagic larval duration, and planktivore populations.

Plain Language Summary

Winds blowing parallel to a coastline push the surface layer of the ocean away from shore, thereby pulling up deeper, cooler water in a process called “upwelling”. In the Red Sea, an

45 elongated body of water between Africa and the Arabian Peninsula, persistent along-shore winds
46 cause upwelling on shallow-water coral reefs. This process is detectable from satellites orbiting
47 the earth that measure the temperature of the sea surface, but substantial differences exist in the
48 data provided by these satellites. We show which satellites are best suited for characterizing the
49 patterns of upwelling in the Red Sea across time and space by comparing them to an array of
50 temperature loggers deployed underwater. Additionally, our results shed light on how upwelling
51 affects marine life in the Red Sea. For example, this is one of the warmest parts of the world
52 ocean during summer, and the cooling effect of upwelling influences the heat stress experienced
53 by reef-building corals and sea turtles. If temperatures become too high, corals are prone to
54 “bleach” and die, while sea turtle hatchlings become almost all female. Upwelling of cooler
55 water helps to alleviate these stresses, but the winds that drive the upwelling may weaken as the
56 climate changes.

57

1. Introduction

Coral reefs across the tropics have already been heavily degraded by climate change and are expected to become increasingly imperiled as the oceans continue to warm (Hoegh-Guldberg et al., 2014). However, many coral reefs are located in oceanographically complex coastal zones, where temperatures are modulated by a variety of physical processes (Wolanski & Bennett, 1983; Comfort et al., 2019; Davis et al., 2020). While shallow reefs can be sensitive to local amplification of marine heatwaves (Nadaoka et al., 2001; Smith, 2001; Davis et al., 2011; DeCarlo et al., 2017), others are exposed to cooling phenomena such as internal waves, wind-driven and topographic upwelling, storms, and nighttime reprieves from high temperatures (Riegl & Piller, 2003; Leichter et al., 2005; Gove et al., 2006; Wang et al., 2007; Berkelmans et al., 2010; DeCarlo et al., 2015; Green et al., 2019; Reid et al., 2019; Richards et al., 2019). Processes that expose shallow-dwelling corals to deeper water—such as internal waves and upwelling—can sometimes mitigate bleaching (Schmidt et al., 2016; DeCarlo et al., 2017; Wyatt et al., 2019), but also have the potential to exacerbate stress due to different nutrient, pH, and oxygen levels (Leichter et al., 2003; Barkley et al., 2018; DeCarlo & Harrison, 2019). The transport of sub-thermocline waters toward the surface also tends to have large ecological ramifications in reef ecosystems, such as fueling algal blooms (van Woesik, 2004), diminishing coral diseases (Rodríguez & Cróquer, 2008), and weakening coral reef cementation (Manzello et al., 2008).

In many cases, the localized processes that cool reef environments are not included in assessments of reef health or coral bleaching that are based on remote sensing. This is primarily because these processes are often sub-gridscale—meaning that they occur on spatial scales that are too small, timescales that are too short, or in habitats that are too deep to be resolved in

gridded sea surface temperature (SST) datasets (Wolanski & Pickard, 1983; Wang et al., 2007; Benthuisen et al., 2016; Wyatt et al., 2019). Yet, exceptions exist. For example, the highest-resolution (4-km) SST datasets have been used to resolve topographic upwelling of the Equatorial Undercurrent onto coral reefs in the central Pacific Ocean (Karnauskas & Cohen, 2012) and the internal-wave surf zone on Dongsha Atoll in the South China Sea (Reid et al., 2019). Additionally, wind-driven upwelling, which occurs in coral reef areas such as the eastern tropical Pacific and South Africa (Wellington et al., 2001; Riegl & Piller, 2003; Chollett et al., 2010), tends to occur on large enough temporal and spatial scales to be resolved by satellite-based SST products.

In the Red Sea, upwelling has received relatively little attention, particularly in coral reef habitats. Patzert (1974) noted that monsoon wind reversals could induce vertical mixing and upwelling, particularly in the far northern Red Sea. Churchill et al. (2014) traced the inflow of cool, nutrient-rich, sub-surface Gulf of Aden Intermediate Water (GAIW) into the Red Sea, and noted that it is mainly constrained to the eastern margin of the southern Red Sea. Their observations of GAIW extended to the shelf edge but not onto the shelf where coral reefs are abundant (Fig. 1). Other studies have described the influx of nutrients in the southern Red Sea and resulting plankton blooms (Raitsos et al., 2015; Dreano et al., 2016; Pearman et al., 2017), but without characterizing the dynamics of upwelling within the Red Sea. Antonius (1988) first mentioned that high-nutrient Indian Ocean water impacts the Farasan Islands, but to our knowledge, no study has investigated the spatio-temporal patterns, and the drivers, of upwelling onto the shelf and across coral reef habitats in the southern Red Sea.

Here, we use an array of *in situ* temperature loggers deployed during 2015-2019 in coral reef habitats of the Farasan Banks to describe the spatial and temporal patterns of upwelling. We

test (1) if spatial patterns of upwelling across the shelf exist, (2) which satellite SST products are most effective for capturing the spatial and temporal patterns of upwelling, and (3) if the temporal variability of upwelling is related to the wind field. Additionally, we define regions of the Red Sea clearly affected by upwelling, those unaffected by upwelling, and a transition zone between the two. Finally, we explore the ecological implications of the upwelling, including its effects on coral bleaching, turtle nesting, biodiversity, and plankton blooms.

2. Methods

2.1. Temperature loggers

We deployed and recovered temperature loggers at a total of 40 locations in the Farasan Banks region (Fig. 1). The majority of loggers (28) were deployed either in February or May 2019 until February 2020 to capture the 2019 period of early-summer upwelling (typically June-September) and late-summer maximum temperatures (typically September-October). Two other loggers were deployed in May 2015 and recovered in January and May 2017. A new logger was re-deployed at one of these locations in August 2017, along with two additional loggers at different locations near the coast (exact locations of loggers in each year are displayed in subsequent figures). Another nine loggers were deployed in early 2018. The five loggers deployed in 2015 and 2017, and two of the loggers deployed in each of 2018 and 2019, were Onset Temp Pro v2 (U22-001) models, which have a factory-stated accuracy of 0.21 °C. One logger deployed in 2018 was an Onset TidbiT (UTBI-001), which also has a factory-stated accuracy of 0.21 °C. The other loggers were Onset Pendant (UA-001-64) models, which have a factory-stated accuracy of 0.53 °C. All three models have a maximum drift of 0.1 °C per year. The accuracy of Onset loggers can be significantly improved by calibrating them in an isothermal bath prior to deployment

(Lentz et al., 2013). All of the loggers that we deployed in 2019, and one of the Pendant loggers deployed in 2018, were calibrated beforehand in a Fluke 7012 temperature bath with a Fluke 1504 temperature display and an ES225 thermistor probe. The calibration was conducted in 5 °C increments between 20 °C and 40 °C (or 15 °C to 35 °C in 2018), allowing at least one hour of equilibration at each temperature. Although the offsets (y-intercepts) between the loggers and the bath temperatures were as large as 0.3 °C for Pendant loggers, the averaged difference between the bath temperature and the calibrated logger temperatures ranged from only 0.014 °C to 0.041 °C, with an average of 0.028 °C.

Loggers deployed in 2019 were set to record every 15 minutes and were attached to a sub-surface buoy such that the loggers were approximately 1 meter above the bottom at various depths ranging from 1 to 11 meters in coral reef habitats. The loggers deployed earlier recorded at intervals ranging from 15 to 60 minutes, and were attached to either PVC plates or mooring lines at depths of 5 to 28 meters. Our study covered a range of reef types, from fringing reefs along nearshore islands to mid-shelf reef platforms and shelf-edge atolls. Full details of the logger deployments are listed in Supplemental Table S1.

2.2. Remote sensing data

We used a variety of satellite-based SST products for comparison to the *in situ* temperature loggers. These included Optimum Interpolation SST (OI-SSTv2.1) (Reynolds et al., 2007; Banzon et al., 2016), Coral Reef Watch's CoralTemp (CRW) (Liu et al., 2014), and Moderate-resolution Imaging Spectroradiometer (MODIS) (NASA Goddard Space Flight Center, Ocean Ecology Lab). OI-SSTv2.1 and CRW are both daily and of 0.25° and 0.05° (~25 km and ~5 km) resolution, respectively. For MODIS, we used both the Terra and Aqua satellites, and for each of

these we used the longwave data for both day and night, and the shortwave data (only valid at nighttime). All of the MODIS data are 4-km resolution, but the datasets include gaps due to poor quality or clouds (we used data only with quality flags between 0 and 2). We also calculated means of longwave data (averaging day and night) for each satellite, only considering days when there were both day and night data. Similarly, we calculated longwave and shortwave means (averaging Terra and Aqua), but retained days when only data from one satellite was available.

We acquired wind speed data (~25-km resolution) from the European Centre for Medium-Range Weather Forecasts (ECMWF) ERA5 dataset (Copernicus, 2017). To compare wind fields to upwelling events during the temperature logger deployments, we used the 10-m altitude hourly wind speed data, which we averaged to daily means. For longer-term assessments of wind speed anomalies, we used monthly averaged data from 1979-2019. Additionally, we used heat flux data from ERA5 to describe the processes leading to coral bleaching in 2015. These data included monthly means of latent, solar, longwave, and sensible heat fluxes. Finally, we used ERA5 monthly mean air temperature (2-m altitude) data to investigate the relationship between water and air temperatures. For all monthly datasets, we calculated monthly anomalies relative to the 1982-2012 monthly climatological base period.

To describe the oceanographic changes associated with the monsoon winds in the southern Red Sea, we used sea surface height (SSH) anomalies from the Archiving, Validation and Interpretation of Satellite Oceanographic data (AVISO) group. SSH data were visualized by removing the daily climatological (1993-2018) mean of the entire southern Red Sea (south of 21°N). This was done because sea level variations in the Red Sea are dominated by a seasonal pattern (Churchill et al., 2019) that would obfuscate shorter-term and spatial variations.

2.3. Coastline and bathymetry data

We used the high-resolution coastline data from Wessel and Smith (1996) and the 1-minute bathymetry data from Amante and Eakins (2009). We defined the shelf edge as the 100-m isobath.

2.4. Logger-satellite mismatch descriptive statistics

To characterize the differences in mean daily temperatures between satellite-derived SST and the *in situ* temperature loggers, we used descriptive statistics including Bias (satellite – logger mean), Root Mean Square Error (RMSE), and the coefficient of determination (r^2), which were calculated separately for each temperature logger and for each satellite product. Bias shows the overall offset, RMSE represents the deviations from a 1:1 line after accounting for bias (*i.e.*, we first subtracted the bias from the satellite and then calculated RMSE), and r^2 signifies the correlation between the two datasets irrespective of deviations from a 1:1 line. Thus, a better match between satellites and loggers is indicated by a bias and RMSE close to 0, and r^2 close to 1. These calculations were only performed using the Temp Pro, TidbiT, or calibrated Pendant logger data (*i.e.*, we did not use uncalibrated Pendant logger data).

We calculated daily temperature range as the difference between the maximum and minimum temperature recorded by each logger per day (Safaie et al., 2018), and then we averaged the temperature range of all days to determine the mean daily temperature range per logger.

2.5. Quantifying upwelling and heat stress

We quantified upwelling and heat stress based on maximum and minimum temperatures during certain time periods, as described below. Therefore, as an initial step, we calculated 7-day running means of all temperature datasets (loggers and satellite products) in order to avoid spurious results from single anomalous days, and these running means were used in all subsequent calculations.

Upwelling was quantified as the change in temperature from the maximum during a certain time interval to the minimum during a subsequent interval. During 2019, these time intervals were selected after inspecting the data and were chosen to highlight certain events. The first upwelling event began early in the season around 20 April, and we quantified this as the difference between the minimum temperature over 20-30 April and the preceding maximum temperature during 10-20 April. The sustained upwelling period began around 12 June, and for this event we calculated the difference between the minimum temperature over 12-30 June and the maximum temperature during 1-12 June. For most temperature loggers, the lowest temperatures during the upwelling season were reached in July, so we quantified the final interval as the minimum July temperature relative to the same 1-12 June maximum used in the previous time interval. For the analysis of interannual differences in upwelling, we did not select intra-seasonal events, but rather quantified the maximum intensity of upwelling per year as the difference between the minimum temperature at any time during June to August and the maximum temperature in June. Since no temperature loggers were deployed during June 2017, we did not include the 2017 upwelling season in our analysis. All of these calculations were performed for both satellite-derived SST and the *in situ* temperature loggers. We used all loggers in these calculations, including uncalibrated Pendant logger data, because the logger calibrations

primarily corrected offsets in the mean of each logger, and these corrections do not affect upwelling and heat stress calculations.

Maximum heat stress per year (which typically occurs in September-October) was calculated following common techniques to quantify coral reef heat stress (Liu et al., 2003). We calculated the maximum monthly mean (MMM) by building monthly climatologies for each grid-box using a 1982-2012 base period and selecting the month with the highest monthly mean. Heat stress was then calculated as the maximum 7-day running mean temperature above the MMM. For temperature loggers, we used the MMM of the nearest grid-box and subtracted the satellite-logger bias when calculating heat stress. The maximum heat stress per year was then calculated for both satellites and temperature loggers during 2015, 2016, 2018, and 2019.

We compared the upwelling intensity and maximum heat stress for the time periods described above between satellite-derived SST and temperature loggers. To do this, we extracted only the satellite data for the single grid-box nearest to each temperature logger, and we report the RMSE and r^2 between satellites and loggers for the spatial patterns of upwelling and heat stress.

3. Results and Discussion

3.1. Satellite-logger temperature mismatches

Our temperature logger array in the Farasan Banks spanned approximately 6,000 km² (equivalent to ~40% of the Farasan Banks area), covering coral reef habitats from shelf-edge atolls to nearshore fringing reefs. Comparisons between temperature logger and satellite-derived SST data clearly indicate that each satellite product had a negative bias relative to every temperature logger (Fig. 2A). This means that, on average throughout our deployments, all of the satellite

SST products underestimated the temperatures of coral-reef waters. The median bias of OI-SSTv2.1 was closer to zero than all other satellite products, although it was still -0.54 °C. Our observed offsets are relatively large compared to satellite-logger assessments in coral reef regions outside of the Red Sea, except for a few instances of larger biases in isolated embayments, on shallow reef flats, or on internal wave-exposed reefs (Wellington et al., 2001; Aronson et al., 2002; Strong et al., 2002; Castillo & Lima, 2010; DeCarlo et al., 2016, 2017; Pan et al., 2017; Benthuisen et al., 2018; Claar et al., 2019; DeCarlo & Harrison, 2019). We found the largest negative biases for the shallowest loggers with high daily temperature ranges, but even loggers at 20 m depth or greater were consistently warmer than satellite SST products (Fig. 3). Likewise, Hume et al. (2020) reported similar cool biases (~0.5 to >1°C) in satellites compared to reef temperatures across the shelf in the Thuwal area of the central Red Sea, approximately 300 km north of the Farasan Banks. Together, this suggests that satellite-derived SST in portions of the Red Sea may substantially underestimate reef-water temperatures.

Despite the relatively large biases in absolute temperatures, satellites tracked variations in temperature comparably well. For instance, the median RMSE of 0.38 and 0.50 °C for CRW and OI-SSTv2.1 (Fig. 2B) are near the lower end of the range of those reported for these two products on the Great Barrier Reef of Australia (DeCarlo & Harrison, 2019). This indicates that CRW and OI-SSTv2.1 can reliably record temperature variations and anomalies, even though a bias correction is required for accurate absolute temperatures. The MODIS products were consistently worse than CRW and OI-SSTv2.1, except that their r^2 values were in some cases better than OI-SSTv2.1 (Fig. 2). However, there were some patterns within the subsets of MODIS data. The mean of longwave day and night data was generally better in all three metrics relative to day or night data alone (Fig. 2). Conversely, averaging Terra and Aqua data did not

substantially improve any of the metrics, and in some cases led to worse results than Terra or Aqua on their own (Fig. 2). Finally, the MODIS shortwave data were consistently better than the longwave data in terms of RMSE and r^2 (Fig. 2). Castillo and Lima (2010) compared MODIS longwave day and night data to *in situ* temperature loggers on the Mesoamerican reef of Belize. They reported consistent negative biases only in the nighttime data, but not in the daytime data. Additionally, they found better correlations and lower RMSE for daytime data compared to nighttime. Our results differ from Castillo & Lima (2010) in that longwave MODIS nighttime performed better than daytime data in all metrics, and biases were always negative (for both day and night), which suggests that the reliability of MODIS products for detecting reef temperatures may vary around the world.

At least some of the variations among loggers in Bias, RMSE, and r^2 were related to either depth or diurnal temperature variability (Fig. 3). Loggers deployed deeper recorded smaller daily temperature ranges (Fig. 3A), making these two factors difficult to disentangle. Nevertheless, CRW, OI-SSTv2.1, and MODIS shortwave (excluding the other MODIS data for simplicity) all have more negative biases for loggers with greater daily temperature ranges (or that were deployed shallower) (Fig. 3B). Likewise, RMSE increased, and r^2 decreased, with increasing daily temperature range, except for MODIS (Fig. 3C,D). These results indicate that the performance of satellite products was even better (lower RMSE, higher r^2 , and bias closer to 0) for deeper (5-30 m), more thermally stable reef habitats (Fig. 3). Although it is intuitive that deeper loggers would record cooler temperatures, it is surprising that even at 20 m or deeper, we still find warmer *in situ* temperatures than satellite SST. This differs from a study of *in situ* temperatures on reefs across the Pacific Ocean, where loggers deployed at 20 m depth in coral reef environments were consistently cooler than the SST derived from satellites (Wyatt et al.,

2019). There are at least two possible explanations for this. First, the SST-logger offsets are so large in the Red Sea that even though deeper loggers are in cooler waters, the difference is not great enough to overcome the satellites' cool biases. Second, loggers deployed at 20 m or deeper across the Pacific are frequently cooled by internal waves (Wyatt et al., 2019; Davis et al., 2020), which are either absent or of small magnitude in the Red Sea.

The patterns in skill among the satellite SST products do not follow their differences in spatial resolution. Although MODIS offers the highest spatial resolution of 4 km, most subsets of the MODIS data (*e.g.*, nighttime) performed relatively poorly (Fig. 2). Only MODIS shortwave data were of similar quality to OI-SSTv2.1 and CRW. Although CRW is relatively high resolution (~5 km) and performed the best in terms of RMSE and r^2 , this may have more to do with its use of multiple satellite sensors rather than spatial resolution (Liu et al., 2014), since 4-km MODIS data were even more different from the logger data (Fig. 2). Additionally, OI-SSTv2.1 had the Bias closest to zero, despite having the lowest spatial resolution (~25 km). Thus, higher spatial resolution in a satellite SST product does not necessarily translate to greater accuracy or precision.

3.2. Spatial and temporal patterns of upwelling across the shelf

During 2019, the first cooling event in late-April was most strongly detected (*i.e.*, the largest drop in temperature) in loggers closest to the shelf edge (Fig. 4A,E,I). A similar pattern also occurred at the onset of the main upwelling period beginning 12 June (Fig. 4B,F,J). The spatial pattern reversed by July, when the strongest cooling was concentrated in loggers located nearshore and northward (Fig. 4C,G,K).

We tested the skill of the satellite products in representing these spatial patterns (Fig. 4). MODIS performed poorly for capturing the spatial patterns of upwelling, especially in June and July, when there was nearly no correlation ($r^2 < 0.15$) between MODIS and the loggers in degree of upwelling (Fig. 4B-C). Even though MODIS shortwave performed reasonably well in terms of Bias, RMSE, and r^2 for the overall satellite-logger comparisons (Fig. 2), our spatial analysis clearly shows that MODIS is unreliable for tracking the spatial variability of specific upwelling events in the Farasan Banks (Fig. 4A-C). This is due to a combination of missing data, particularly at the start of the upwelling period in mid-June, and frequent spuriously cold days throughout the summer that were several °C cooler than the logger data (Fig. 4D). Conversely, CRW and OI-SSTv2.1 more successfully tracked spatial patterns in upwelling across the shelf. Despite some discrepancies with the loggers, both CRW and OI-SSTv2.1 correctly showed more intense upwelling near the shelf edge in April and June, switching to stronger upwelling along the coast in July (Fig. 4E-G,I-K). Unlike the long-term bias (Fig. 2A), satellite detection of upwelling did not produce consistently negative offsets. This reinforces our conclusion that at least some satellite products are capable of tracking SST changes (*e.g.*, upwelling events) even if the long-term mean temperatures are offset from *in situ* loggers. Further, even though CRW was the best in the long-term RMSE and r^2 statistics (Fig. 2), OI-SSTv2.1 consistently outperformed (Bias nearer to zero, lower RMSE, and higher r^2) CRW at capturing the spatial patterns of upwelling in 2019 (Fig. 4). This finding is surprising since 25 CRW grid-boxes fit within a single OI-SSTv2.1 grid-box, and it provides additional evidence that higher spatial resolution does not necessarily translate to improved skill in detecting spatial or temporal variability.

Satellite SST products indicate substantial interannual variability in the intensity of upwelling, a pattern that was corroborated by our temperature loggers (Fig. 5). Both CRW and

331 OI-SSTv2.1 show strong upwelling during 2015, reaching as much as 3 °C cooling nearshore
332 (Fig. 5 E-L). However, despite the intense upwelling signal in both of these satellite products
333 during 2015, even this is underestimated since our nearshore temperature loggers recorded as
334 much as 5°C cooling. During both 2015 and 2016, upwelling intensity clearly increased toward
335 the coast, whereas upwelling during 2018 and 2019 was more evenly distributed or even greater
336 near the shelf edge. Although the lack of temperature loggers across the shelf during these earlier
337 years prohibits validation of these patterns, the ability of CRW and OI-SSTv2.1 to detect the
338 spatial patterns of upwelling during 2019 suggests that the interannual variability in spatial
339 upwelling patterns likely reflect reality.

340 Detection of upwelling through the use of satellite-based SST products is common in
341 coastal boundary currents (*e.g.*, Nykjaer & Van Camp, 1994; Demarcq & Faure, 2000; Kuo et
342 al., 2000; Goubanova et al., 2013; Benazzouz et al., 2014), including in some coral reef areas
343 (*e.g.*, Glynn, 1993; Kleypas & Burrage, 1994; Taylor & Pearce, 1999; Hénin & Cresswell, 2005).
344 However, validation of satellite-derived upwelling patterns with *in situ* measurements is less
345 common (but see *e.g.*, Glynn & Leyte Morales, 1997; Wellington et al., 2001; Tang et al., 2002;
346 Berkelmans et al., 2010). Additionally, few studies compare the utility of multiple satellite SST
347 products for characterizing coral-reef water temperatures (but see Castillo & Lima, 2010;
348 DeCarlo & Harrison, 2019). Thus, the combination of our temperature logger array and
349 comparison to multiple satellite SST products demonstrates the need to carefully choose SST
350 data and to validate their skill at detecting the parameter of interest (*e.g.*, upwelling or maximum
351 temperatures).

352 353 3.3. Physical drivers of upwelling in the Farasan Banks

Our temperature loggers deployed in coral reef habitats of the Farasan Banks during 2019 all recorded the same dominant pattern of cooling during the upwelling season between June and August, albeit with differences in the mean and in short-term variations (Fig. 6A). All loggers show a sharp decline in temperature beginning within a few days of 12 June, ranging in magnitude from ~1-3 °C. This upwelling period, characterized by cool temperatures relative to the early-June maxima, lasted until early September, after which temperatures began to rise again until reaching maxima in early October. An earlier cooling event also occurred in late April that was recorded by some, but not all loggers.

Comparison of wind fields with our temperature logger time series reveals that the Farasan Banks upwelling is wind-driven (Fig. 6). The short-lived April 2019 cooling event coincided precisely with a 5-day wind burst toward the southeast. Likewise, the onset of sustained upwelling in mid-June 2019 occurred exactly when the summer monsoon began. Beginning 12 June, winds switched from relatively weak and of variable direction to comparably strong (typically exceeding 10 m s^{-1} daily mean) and consistently toward the southeast until early- to mid-September (Fig. 6A). These southeast-ward winds are upwelling favorable for the eastern side of the basin, including Farasan Banks, because Ekman transport is directed away from the coast. Similar along-shore winds drive upwelling in other coral reef regions such as New Caledonia (Hénin & Cresswell, 2005) and Colombia (Chollett et al., 2010). However, it is important to note that not all coral-reef upwelling systems are wind driven, as along-shore currents can also drive upwelling, for example in Madagascar (Chollett et al., 2010) and the central Great Barrier Reef (Benthuisen et al., 2016; DeCarlo & Harrison, 2019).

The process by which Ekman transport drives upwelling in the Farasan Banks is evident in SSH anomalies corresponding to the wind field (Fig. 6B-J). Prior to the late-April wind burst,

SSH was relatively high around the Farasan Banks (Fig. 6B), decreased during the wind burst from 19 to 23 April (Fig. 6C), and then returned to unusually high levels by early June (Fig. 6D). When the monsoon winds began during 12-16 June, SSH became low on the eastern side of the basin but relatively high on the western side (Fig. 6E). This pattern persisted through July (Fig. 6F) and August, with occasional respites (*e.g.*, Fig. 6G). The common pattern of low SSH on the east and high SSH on the west during southeast-ward winds persisted until early-September (Fig. 6I), returning to anomalously high SSH in October when the wind direction switched back to northwest-ward (Fig. 6J). Thus, during the monsoon season, SSH lows are generally associated with the eastern side of the basin, consistent with the notion that the southeast-ward winds transport water 90° to the right of the wind direction, away from the coast and toward the western side of the basin. This net transport leads to upwelling as deeper waters are pulled to the surface to replace the surface waters. Indeed, times of strong southeast-ward winds are linked not only with SSH lows near the Farasan Banks, but also with sharp declines in temperature, as recorded by our *in situ* loggers (Fig. 6A).

Winds blowing into the Red Sea through the Tokar Gap play a key role in the wind climate of the southern Red Sea, especially during July and August (Jiang et al., 2009; Ralston et al., 2013; Viswanadhapalli et al., 2017). While intermittent wind bursts through the Tokar Gap may cause some upwelling on parts of the western side of the Red Sea, they do not appear to substantially modify the wind-driven upwelling in the Farasan Banks (Fig. 6H). At these times, the wind direction in the Farasan Banks becomes more east-ward than southeast-ward, but the pattern of SSH lows in the Farasan Banks, and sustained cooling (Fig. 6A), indicates that upwelling still occurs. Rather, it is the monsoon winds blowing along the main axis of the Red Sea that appear to be the dominant driver of upwelling in the Farasan Banks.

The same pattern of wind-driven upwelling occurred in 2015, with the onset of the monsoon winds in mid-July sparking SSH lows and sharply declining temperatures in the Farasan Banks (Fig. 7). However, this analysis does not offer a clear explanation for the much greater upwelling intensity during 2015 compared to 2019 (Fig. 5). Neither the wind strength, nor the SSH pattern, appears anomalous during 2015 relative to 2019 (Fig. 6B-J, Fig. 7B-D). One possible explanation is that the more intense upwelling during 2015 resulted from more sustained, rather than stronger, winds. There was no break in the monsoon winds from the start of upwelling in mid-June through the end of July 2015 (Fig. 7A), whereas winds and upwelling both declined during a short period in late-June 2019 (Fig. 6A). Alternatively, it is possible that other factors led to the greater cooling during 2015. For instance, it is conceivable that GAIW, which is the coolest water found in the Red Sea (Sofianos & Johns, 2007; Churchill et al., 2014), was more prevalent or closer to the surface during 2015 than 2019, although we are unable to test this hypothesis.

The monsoon winds in the Red Sea that drive upwelling in the Farasan Banks are connected to the larger-scale southwest Indian monsoon (Pearman et al., 2017; Attada et al., 2019). Low-pressure systems over southern Asia force surface winds across much of the Indian Ocean, including the Red Sea, toward the Indian subcontinent. This same process drives the better-known upwelling in the Arabian Sea off the coast of Oman during the summer months (Currie et al., 1973; Burt et al., 2016). The influence of the southwest Indian monsoon on southern Red Sea winds is evident in correlation maps between wind speed anomalies in the Farasan Banks and the broader Arabian Sea region (Fig. 8). Only weak correlations exist in July (Fig. 8A), with the clear link between the southwest Indian monsoon and the Red Sea developing in August (Fig. 8B) and peaking in September (Fig. 8C). Wind bursts through the Tokar Gap,

although locally important (Ralston et al., 2013), do not play a major role in this process since weak or negative correlations occur between wind speed anomalies in the Farasan Banks and the coastal area in front of the Tokar Gap during July and August. Thus, understanding the Red Sea summer monsoon and its interannual variability requires a broader perspective that includes the Arabian Sea and the southwest Indian Monsoon.

3.4. Cause of the 2015 heat anomaly

The greatest heat stress during the course of our study occurred in 2015, when temperature anomalies relative to the maximum monthly mean (MMM) reached approximately 2 °C (Fig. 9). These high-temperature anomalies were generally tracked by both loggers and satellites, although the satellites consistently underestimated the peak temperature anomalies (Fig. 9). That such high temperatures occurred in the Farasan Banks during 2015 is initially surprising since this same area was cooled by unusually strong upwelling earlier in the summer (Fig. 5).

Our analysis of winds and SSH did not identify a clear cause of the exceptionally strong 2015 upwelling, but it does reveal a key anomaly in the 2015 monsoon season. Unlike in 2019, when the monsoon winds lasted until mid-September, the monsoon effectively ended at the beginning of August in 2015. Afterwards, there were occasional weak southeast-ward winds, but not sustained monsoon winds (Fig. 7A). Indeed, the August wind speeds in the Farasan Banks during 2015 were the lowest since at least 1979 (Fig. 10A). Since the reef-water temperatures in the Farasan Banks begin rising immediately after the cessation of persistent monsoon winds, the late-summer warming period was anomalously long in 2015. For example, the late-summer warming period in 2019 lasted only one month, from mid-September to mid-October (Fig. 6A),

whereas reef-water temperatures rose near-continuously for two months in 2015, during all of August and September (Fig. 7A).

The progression of the unusual 2015 monsoon season is apparent in wind-speed anomaly maps of the broader Arabian Sea region (Fig. 8). During July, when Farasan Banks winds are mostly controlled locally without broad-scale teleconnections (Fig. 8A), anomalously high wind speeds occurred in most of the southern Red Sea (Fig. 8D), which may have contributed to the strong 2015 upwelling signal. Conversely, during August and September, when southern Red Sea winds are largely controlled by remote forcing from the Arabian Sea (Fig. 8B-C), there were anomalously weak winds extending all the way from the southern Red Sea across the Arabian Sea to the Indian subcontinent (Fig. 8E-F). Indeed, the 2015 southwest Indian monsoon was unusually weak, causing severe droughts in India (Mishra et al., 2016). Broader analyses of Pacific wind fields suggest that the Indian monsoon is modulated by changes in Indo-Pacific atmospheric circulation established by El Niño conditions (Joseph et al., 1994), and that the particularly weak 2015 Indian monsoon was caused by the strong El Niño that year (Kakatkar et al., 2018).

The early cessation of the monsoon winds leads to warming of reef waters in Farasan Banks through two mechanisms. First, without the monsoon winds, upwelling stops, thus eliminating this cooling mechanism. Second, the heat budget of the Red Sea is dominated by warming from shortwave (solar) radiation and cooling from latent heat flux (primarily evaporation), with the latter mainly controlled by wind speed. A reduction in wind speed reduces the evaporative cooling effect, leading to greater heating of the Red Sea. Consistent with this notion, August 2015 wind speeds were anomalously low (Fig. 10A), and both the latent and total heat flux anomalies during 2015 for the month of August were the highest on record (Fig. 10B).

Conversely, while the September 2015 total heat flux was still anomalously high (Fig. 10C), it was not exceptionally so, even though the peak temperatures were reached at the end of September. Across all years from 1979-2019, wind speeds were strongly correlated with both latent heat flux anomalies ($r^2 = 0.72$ for August, $r^2 = 0.77$ for September) and total heat flux anomalies ($r^2 = 0.62$ for August, $r^2 = 0.72$ for September). In both August and September, the anomalously high total heat fluxes were primarily driven by latent heat flux—due to reduced winds—rather than strong anomalies in solar or longwave radiation, or sensible heat flux. Therefore, we interpret the exceptionally high temperatures in 2015 recorded by both satellites and *in situ* temperature loggers (Fig. 8) as arising primarily from a longer duration late-summer warming period rather than exceptionally strong instantaneous heat fluxes. This differs from the drivers of other marine heatwaves in coral reef regions. For example, the 2016 marine heatwave on the Great Barrier Reef was caused primarily by anomalously high instantaneous solar radiation, with little contribution from latent heat flux (Benthuisen et al., 2018; Karnauskas, 2020)

3.5. Spatial extent of summertime upwelling in the Red Sea

Based on our observations here, we can define the areas of the Red Sea shelf (<100 m depth) that are exposed to summertime upwelling (Fig. 11). We define the main upwelling zone as shelf areas where the climatological minimum daily mean SST in July is less than the climatological maximum daily mean SST in June. This zone is exclusively located on the eastern margin of the southern Red Sea, extending from the northern Farasan Banks southward to the Farasan Islands, ending near the border between Saudi Arabia and Yemen. The location of this zone is consistent with the notion that the upwelling is wind-driven, as Ekman transport in response to southeast-

ward winds is only upwelling-favorable on the eastern shelf. Conversely, a non-upwelling zone has its peak climatological SST in August, and follows a more regular sinusoidal seasonal pattern. Summertime upwelling is absent along the entire northern half of the Red Sea and a portion of the Eritrea coastline south of the Tokar Gap. Finally, there is a transition zone between the upwelling and non-upwelling criteria. SST in this zone does not follow a sinusoidal seasonal pattern, but rather has a more saw-toothed seasonal SST cycle, with a delayed peak in September. This zone is clearly influenced by the monsoon winds in that the rate of warming slows at the same time the monsoon begins in June, however, there is not a dip in temperature below the June maximum. This zone covers the outer shelf areas of the Farasan Banks and Farasan Islands, and much of the western margin of the southern Red Sea. The transition zone is not necessarily exposed to regular upwelling, but may rather have reduced rates of warming in early summer due to evaporative cooling during the monsoon period. Additionally, the transition zone seems to include areas, such as the outer-shelf Farasan Banks, that are exposed to upwelling in some years, but not consistently enough to cause a dip in the climatological temperatures from June to July. We suggest that these criteria provide a simple zonation of the Red Sea that can be useful in defining a range of ecological characteristics such coral bleaching sensitivities and nutrient exposure, whereas previous considerations of Red Sea zonation have focused on faunal distributions (*e.g.*, Spalding et al., 2007; Roberts et al., 2016; Berumen et al., 2019).

3.6. Ecological implications

Upwelling in the southern Red Sea has potentially broad ecological implications such as modulating coral bleaching, defining turtle sex ratios, shaping species composition and biodiversity patterns, fueling phytoplankton blooms, influencing fish pelagic larval durations,

and establishing manta ray feeding habitats. These non-exhaustive examples are discussed briefly below.

As described above, exceptionally high temperatures occurred in the Farasan Banks in late-summer (September and October) 2015, which initiated a devastating coral bleaching event (Osman et al., 2018). The high temperatures in 2015 resulted from an early end to the monsoon that year (Figs. 8-10), and crucially, this heat stress came on the heels of unusually intense upwelling in June and July (Fig. 5). Since corals are more susceptible to bleaching after exposure to high nutrients (Cunning & Baker, 2012; Wiedenmann et al., 2013), the combination of strong upwelling of nutrient-rich waters followed by heat stress likely exacerbated the bleaching response. However, at other times, upwelling may have spared Farasan Banks corals from bleaching. For example, the first observed Red Sea mass coral bleaching event in 1998 spanned from Yemen, Eritrea, and Sudan in the south to the Thuwal region of Saudi Arabia and southern Egypt in the central to northern Red Sea (Devantier & Pilcher, 2000; Devantier et al., 2000; Osman et al., 2018). The Farasan Banks were one of the few regions of the Red Sea apparently not affected by bleaching in 1998 (Osman et al., 2018). One potential reason for the lack of bleaching at this time was that upwelling mitigated heat stress. Wind speeds were anomalously low in August and September 1998, likely due to the effect of El Niño on the Indian summer monsoon, but not nearly as low as in 2015 (Fig. 10). Therefore, upwelling continued cooling the Farasan Banks throughout the summer of 1998 more than the summer of 2015, potentially creating a temporary refuge from the high temperatures, and therefore bleaching, that impacted reef areas elsewhere in the Red Sea.

The effective removal of the top of the SST peak in the upwelling region of the Red Sea (Fig. 11) could influence a broader range of organisms beyond corals. For example, the

summertime upwelling in the Farasan Banks and Farasan Islands could have benefits to the local sea turtle populations. The southern Red Sea is an important nesting site for the endangered hawksbill (*Eretmochelys imbricata*) and green turtle (*Chelonia mydas*), and nesting primarily coincides with the summer months (Mancini et al., 2015). Marine turtles demonstrate temperature-dependent sex ratios, meaning that eggs incubated at their pivotal temperature (~29 °C depending on geographic location and species) produce a 50:50 sex ratio, and temperatures above this threshold produce predominantly females (Mrosovsky, 1994). Further, consistent nest temperatures above 33 °C can result in morphological abnormalities and hatchling mortality (Packard et al., 1977; Glen et al., 2003; Hawkes et al., 2007; Laloë et al., 2017). Turtle nesting sites in the southern Red Sea are not exposed to other cooling mechanisms found at some turtle nesting sites elsewhere in the world, such as large tidal ranges or rain events (Laloë et al., 2016). Upwelling could play an important role in reducing air temperature, which, along with SST, primarily controls sand temperature (Laloë et al., 2014, 2016, 2017; Bentley et al., 2020). Indeed, maximum monthly mean air temperature (MMM_{air}) in the southern Red Sea follows the same spatial pattern as upwelling with lower temperatures on the eastern side of the basin (Fig. 12A), likely a result of sensible heat exchange. The air overlying turtle nesting sites in the Farasan Banks and Farasan Islands is approximately 1 °C cooler than similar island groups on the western side of the basin (Fig. 12B-C), a difference that could be important both for defining sex ratios and avoiding the dangers associated with incubation above 33 °C.

Upwelling can also potentially modulate species distributions and biodiversity. For example, the southern Red Sea upwelling might have facilitated the colonization of species from the Indian Ocean into the Red Sea (Bowen et al., 2013; DiBattista, Roberts, et al., 2016) by reducing the gradient in maximum temperature that might otherwise act as an environmental

560 barrier to some species' distributions. In lieu of upwelling, the eastern margin of the southern
561 Red Sea would probably experience maximum water temperatures 1-3 °C higher (Fig. 11). By
562 dampening the maximum summer temperatures, upwelling in the southern Red Sea could enable
563 species to more easily cope with the transition from the cooler Gulf of Aden and Indian Ocean
564 into the warmer Red Sea (DiBattista, Choat, et al., 2016). In addition to the effects on
565 temperature, upwelling in the southern Red Sea provides a key source of nutrients to otherwise
566 oligotrophic surface waters (Churchill et al., 2014). The injection of deep, nutrient-rich water
567 into the photic zone plays a crucial role in stimulating phytoplankton blooms in the southern Red
568 Sea and generally establishing a productivity hotspot (Racault et al., 2015; Raitso et al., 2015;
569 Dreano et al., 2016). This higher productivity can benefit fish larvae by providing nutrition
570 during their pelagic phase, leading to enhanced growth and shorter pelagic larval durations
571 (Robitzsch et al., 2016). Plankton blooms in the Farasan Banks region may also be important for
572 sustaining local populations of planktivorous megafauna known to reside seasonally in the
573 northern Farasan Banks such as whale sharks (*Rhincodon typus*) (Cochran et al., 2019) and reef
574 mantas (*Mobula alfredi*) (Braun et al., 2014, 2015). Although beneficial to some taxa, the higher
575 nutrients in the southern Red Sea, particularly nearshore, have been correlated with reductions in
576 the diversity of benthic and planktonic communities (Ellis et al., 2017; Pearman et al., 2017;
577 Carvalho et al., 2019). However, since the low-diversity communities of bacteria and eukaryotes
578 in the nutrient-rich regions of the southern Red Sea are unique (Carvalho et al., 2019), they still
579 contribute to the overall diversity of the Red Sea (*i.e.*, β diversity). Therefore, the effects of
580 upwelling on biodiversity appear to be complex. Upwelling could directly reduce biodiversity of
581 some communities in which only a subset of species benefits from nutrients, but also indirectly

increase biodiversity of the Red Sea by providing a niche for unique communities and reducing the high-temperature barrier at the entrance to the Red Sea.

4. Conclusions

Our analysis of *in situ* temperature loggers and remote sensing data reveals that the eastern shelf of the southern Red Sea is exposed to wind-driven upwelling during the summer monsoon, typically between June and September. In the labyrinth of coral reefs in the Farasan Banks, temperature declines during the upwelling period by as much as 5 °C. The intensity of upwelling varies spatially across the shelf, as well as temporally both intra- and interannually. At least some of the temporal variability is related to the strength and persistence of southeast-ward winds, but the water column thermal structure probably also plays a role. The satellite-based SST products Coral Reef Watch and OI-SSTv2.1 generally capture these spatial and temporal patterns, whereas MODIS is less effective. Counterintuitively, the intensity of early-summer upwelling appears to be decoupled from the maximum summer temperature that occurs in late-summer, which is controlled in part by the timing of the end of the monsoon. The wind-driven upwelling in the southern Red Sea likely plays a key role in providing nutrients to the otherwise oligotrophic surface waters of the Red Sea, and influences a wide range of organisms from plankton to corals, sea turtles, and manta rays. Therefore, continued monitoring and modeling of upwelling in the southern Red Sea will be crucial for understanding the ecological and environmental variability of this region. Finally, this study demonstrates both the complexity and broad spatial scales of how weather anomalies can impact ecological systems in a changing climate, with the unusually strong 2015 El Niño in the Pacific Ocean affecting the monsoon in the Arabian Sea and ultimately causing both drought in India and coral bleaching in the Red Sea.

Data accessibility:

Raw data and code are available at: <https://codeocean.com/capsule/5737391/tree/v1>

Acknowledgements:

We thank Amr Gusti and the crew of the M/Y Dream Master for field assistance. The research reported in this publication was partially supported by funding from a collaboration between KAUST and Saudi Aramco within the framework of the Saudi Aramco – KAUST Center for Marine Environmental Observations (SAKMEO).

Conflict of interest:

The authors declare that there are no conflicts of interest.

Author contributions:

T.M. DeCarlo designed the study, conducted fieldwork, analyzed the data, and led the writing of the manuscript. All other authors contributed to fieldwork or data collection, and critically edited the manuscript.

References

Amante, C., & Eakins, B. (2009). *ETOPO1 1 Arc-Minute Global Relief Model: Procedures, Data Sources and Analysis*. NOAA Technical Memorandum NESDIS NGDC-24.

<https://doi.org/doi:10.7289/V5C8276M>

Antonius, A. (1988). Distribution and dynamics of coral diseases in the Eastern Red Sea. In

Proceedings of the 6th International Coral Reef Symposium, Australia.

Aronson, R. B., Precht, W. F., Toscano, M. A., & Koltés, K. H. (2002). The 1998 bleaching event and its aftermath on a coral reef in Belize. *Marine Biology*, 141(3), 435–447.

<https://doi.org/10.1007/s00227-002-0842-5>

Attada, R., Dasari, H. P., Parekh, A., Chowdary, J. S., Langodan, S., Knio, O., & Hoteit, I. (2019). The role of the Indian Summer Monsoon variability on Arabian Peninsula summer climate. *Climate Dynamics*, 52(5–6), 3389–3404. [https://doi.org/10.1007/s00382-018-4333-](https://doi.org/10.1007/s00382-018-4333-x)

x

Banzon, V., Smith, T. M., Chin, T. M., Liu, C., & Hankins, W. (2016). A long-term record of blended satellite and in situ sea-surface temperature for climate monitoring, modeling and environmental studies. *Earth System Science Data*, 8(1), 165–176.

<https://doi.org/10.5194/essd-8-165-2016>

Barkley, H., Cohen, A., Mollica, N., Brainard, R., Rivera, H., DeCarlo, T., et al. (2018). Repeat bleaching of a central Pacific coral reef over the past six decades (1960–2016).

Communications Biology, 1, 177.

Benazzouz, A., Mordane, S., Orbi, A., Chagdali, M., Hilmi, K., Atillah, A., et al. (2014). An improved coastal upwelling index from sea surface temperature using satellite-based approach - The case of the Canary Current upwelling system. *Continental Shelf Research*, 34, 38–54. <https://doi.org/10.1016/j.csr.2014.03.012>

Benthuisen, J. A., Tonin, H., Brinkman, R., Herzfeld, M., & Steinberg, C. (2016). Intrusive upwelling in the Central Great Barrier Reef. *Journal of Geophysical Research: Oceans*, 121(11), 8395–8416. <https://doi.org/10.1002/2016JC012294>

Benthuisen, J. A., Oliver, E. C. J., Feng, M., & Marshall, A. G. (2018). Extreme marine

warming across tropical Australia during Austral Summer 2015-2016. *Journal of Geophysical Research: Oceans*, 123(2), 1301–1326. <https://doi.org/10.1002/2017JC013326>

Bentley, B. P., Kearney, M. R., Whiting, S. D., & Mitchell, N. J. (2020). Microclimate modelling of beach sand temperatures reveals high spatial and temporal variation at sea turtle rookeries. *Journal of Thermal Biology*, 88, 102522. <https://doi.org/10.1016/j.jtherbio.2020.102522>

Berkelmans, R., Weeks, S. J., & Steinberg, C. R. (2010). Upwelling linked to warm summers and bleaching on the Great Barrier Reef. *Limnology and Oceanography*, 55(6), 2634–2644. <https://doi.org/10.4319/lo.2010.55.6.2634>

Berumen, M. L., Arrigoni, R., Bouwmeester, J., Terraneo, T. I., & Benzoni, F. (2019). Corals of the Red Sea (pp. 123–155). https://doi.org/10.1007/978-3-030-05802-9_7

Bowen, B. W., Rocha, L. A., Toonen, R. J., & Karl, S. A. (2013, June 1). The origins of tropical marine biodiversity. *Trends in Ecology and Evolution*. Elsevier Current Trends. <https://doi.org/10.1016/j.tree.2013.01.018>

Braun, C. D., Skomal, G. B., Thorrold, S. R., & Berumen, M. L. (2014). Diving behavior of the reef manta ray links coral reefs with adjacent deep pelagic habitats. *PLoS ONE*, 9(2), e88170. <https://doi.org/10.1371/journal.pone.0088170>

Braun, C. D., Skomal, G. B., Thorrold, S. R., & Berumen, M. L. (2015). Movements of the reef manta ray (*Manta alfredi*) in the Red Sea using satellite and acoustic telemetry. *Marine Biology*, 162(12), 2351–2362. <https://doi.org/10.1007/s00227-015-2760-3>

Burt, J. A., Coles, S., van Lavieren, H., Taylor, O., Looker, E., & Samimi-Namin, K. (2016). Oman’s coral reefs: A unique ecosystem challenged by natural and man-related stresses and in need of conservation. *Marine Pollution Bulletin*, 105(2), 498–506.

674 <https://doi.org/10.1016/j.marpolbul.2015.11.010>

675 C3S, C. C. C. S. (2017). *ERA5: Fifth generation of ECMWF atmospheric reanalyses of the*

676 *global climate. Copernicus Climate Change Service Climate Data Store (CDS).*

677 Carvalho, S., Aylagas, E., Villalobos, R., Kattan, Y., Berumen, M. L., & Pearman, J. K. (2019).

678 Beyond the visual: using metabarcoding to characterize the hidden reef cryptobiome.

679 *Proceedings of the Royal Society B: Biological Sciences*, 286(1896), 20182697.

680 <https://doi.org/10.1098/rspb.2018.2697>

681 Castillo, K. D., & Lima, F. P. (2010). Comparison of in situ and satellite-derived (MODIS-

682 Aqua/Terra) methods for assessing temperatures on coral reefs. *Limnology and*

683 *Oceanography: Methods*, 8(3), 107–117. <https://doi.org/10.4319/lom.2010.8.0107>

684 Chollett, I., Mumby, P. J., & Cortés, J. (2010). Upwelling areas do not guarantee refuge for coral

685 reefs in a warming ocean. *Marine Ecology Progress Series*, 416, 47–56.

686 Churchill, J. H., Bower, A. S., McCorkle, D. C., & Abualnaja, Y. (2014). The transport of

687 nutrient-rich Indian Ocean water through the Red Sea and into coastal reef systems. *Journal*

688 *of Marine Research*, 72(3), 165–181. <https://doi.org/10.1357/002224014814901994>

689 Churchill, J. H., Davis, K., Wurgaft, E., & Shaked, Y. (2019). Environmental setting for reef

690 building in the Red Sea. In M. L. Berumen & C. R. Voolstra (Eds.), *Coral Reefs of the Red*

691 *Sea* (pp. 11–32). https://doi.org/10.1007/978-3-030-05802-9_2

692 Claar, D. C., Cobb, K. M., & Baum, J. K. (2019). In situ and remotely sensed temperature

693 comparisons on a Central Pacific atoll. *Coral Reefs*, 38(6), 1343–1349.

694 <https://doi.org/10.1007/s00338-019-01850-4>

695 Cochran, J. E. M., Braun, C. D., Cagua, E. F., Campbell, M. F., Hardenstine, R. S., Kattan, A., et

696 al. (2019). Multi-method assessment of whale shark (*Rhincodon typus*) residency,

distribution, and dispersal behavior at an aggregation site in the Red Sea. *PLOS ONE*, 14(9), e0222285. <https://doi.org/10.1371/journal.pone.0222285>

Comfort, C. M., Walker, G. O., McManus, M. A., Fujimura, A. G., Ostrander, C. E., & Donaldson, T. J. (2019). Physical dynamics of the reef flat, channel, and fore reef areas of a fringing reef embayment: An oceanographic study of Pago Bay, Guam. *Regional Studies in Marine Science*, 31, 100740. <https://doi.org/10.1016/j.rsma.2019.100740>

Cunning, R., & Baker, A. C. (2012). Excess algal symbionts increase the susceptibility of reef corals to bleaching. *Nature Climate Change*, 3(3), 259–262.

Currie, R. I., Fisher, A. E., & Hargreaves, P. M. (1973). Arabian Sea Upwelling (pp. 37–52). Springer, Berlin, Heidelberg. https://doi.org/10.1007/978-3-642-65468-8_4

Davis, K. A., Lentz, S. J., Pineda, J., Farrar, J. T., Starczak, V. R., & Churchill, J. H. (2011). Observations of the thermal environment on Red Sea platform reefs: a heat budget analysis. *Coral Reefs*, 30, 25–36.

Davis, K. A., Arthur, R. S., Reid, E. C., Rogers, J. S., Fringer, O. B., DeCarlo, T. M., & Cohen, A. L. (2020). Fate of internal waves on a shallow shelf. *Journal of Geophysical Research: Oceans*, 125(5), 1–18. <https://doi.org/10.1029/2019JC015377>

DeCarlo, T., & Harrison, H. B. (2019). An enigmatic decoupling between heat stress and coral bleaching on the Great Barrier Reef. *PeerJ*, 7, e7473. <https://doi.org/10.7717/peerj.7473>

DeCarlo, T., Karnauskas, K. B., Davis, K. A., & Wong, G. T. F. (2015). Climate modulates internal wave activity in the Northern South China Sea. *Geophysical Research Letters*, 42(3), 831–838. <https://doi.org/10.1002/2014GL062522>

DeCarlo, T., Gaetani, G. A., Cohen, A. L., Foster, G. L., Alpert, A. E., & Stewart, J. (2016). Coral Sr-U Thermometry. *Paleoceanography*, 31, 626–638.

<https://doi.org/10.1002/2015PA002908>

DeCarlo, T., Cohen, A. L., Wong, G. T. F., Davis, K. A., Lohmann, P., & Soong, K. (2017).

Mass coral mortality under local amplification of 2 °C ocean warming. *Scientific Reports*, 7,

44586. <https://doi.org/10.1038/srep44586>

Demarcq, H., & Faure, V. (2000). Coastal upwelling and associated retention indices derived

from satellite SST. Application to *Octopus vulgaris* recruitment. *Oceanologica Acta*, 23(4),

391–408. [https://doi.org/10.1016/S0399-1784\(00\)01113-0](https://doi.org/10.1016/S0399-1784(00)01113-0)

Devantier, L., & Pilcher, N. (2000). *The status of coral reefs in Saudi Arabia - 2000*.

Devantier, L., Turak, E., Al-Shaikh, K., & De'ath, G. (2000). Coral communities of the central-

northern Saudi Arabian Red Sea. *Fauna of Arabia*, 18, 23–66.

DiBattista, J. D., Roberts, M. B., Bouwmeester, J., Bowen, B. W., Coker, D. J., Lozano-Cortés,

D. F., et al. (2016). A review of contemporary patterns of endemism for shallow water reef

fauna in the Red Sea. *Journal of Biogeography*, 43(3), 423–439.

<https://doi.org/10.1111/jbi.12649>

DiBattista, J. D., Choat, H. J., Gaither, M. R., Hobbs, J.-P. A., Lozano-Cortés, D. F., Myers, R.

F., et al. (2016). On the origin of endemic species in the Red Sea. *Journal of Biogeography*,

43(1), 13–30. <https://doi.org/10.1111/jbi.12631>

Dreano, D., Raitsos, D. E., Gittings, J., Krokos, G., & Hoteit, I. (2016). The Gulf of Aden

Intermediate Water intrusion regulates the southern Red Sea summer phytoplankton

blooms. *PLOS ONE*, 11(12), e0168440. <https://doi.org/10.1371/journal.pone.0168440>

Ellis, J., Anlauf, H., Kürten, S., Lozano-Cortés, D., Alsaffar, Z., Cúrdia, J., et al. (2017). Cross

shelf benthic biodiversity patterns in the Southern Red Sea. *Scientific Reports*, 7(1), 1–14.

<https://doi.org/10.1038/s41598-017-00507-y>

743 Glen, F., Broderick, A. C., Godley, B. J., & Hays, G. C. (2003). Incubation environment affects
 744 phenotype of naturally incubated green turtle hatchlings. *Journal of the Marine Biological*
 745 *Association of the United Kingdom*, 83(5), 1183–1186.
 746 <https://doi.org/10.1017/S0025315403008464h>

747 Glynn, P. W. (1993). Monsoonal upwelling and episodic *Acanthaster* predation as probable
 748 controls of coral reef distribution and community structure in Oman, Indian Ocean. *Atoll*
 749 *Research Bulletin*, 379, 1–66.

750 Glynn, P. W., & Leyte Morales, G. E. (1997). Coral reefs of Huatulco, West México: reef
 751 development in upwelling Gulf of Tehuantepec. *Revista de Biología Tropical*, 45, 1033–
 752 1047.

753 Goubanova, K., Illig, S., Machu, E., Garçon, V., & Dewitte, B. (2013). SST subseasonal
 754 variability in the central Benguela upwelling system as inferred from satellite observations
 755 (1999–2009). *Journal of Geophysical Research: Oceans*, 118(9), 4092–4110.
 756 <https://doi.org/10.1002/jgrc.20287>

757 Gove, J. M., Merrifield, M. A., & Brainard, R. E. (2006). Temporal variability of current-driven
 758 upwelling at Jarvis Island. *Journal of Geophysical Research*, 111(C12).

759 Green, R. H., Lowe, R. J., Buckley, M. L., Foster, T., & Gilmour, J. P. (2019). Physical
 760 mechanisms influencing localized patterns of temperature variability and coral bleaching
 761 within a system of reef atolls. *Coral Reefs*, 38, 759–771. [https://doi.org/10.1007/s00338-](https://doi.org/10.1007/s00338-019-01771-2)
 762 [019-01771-2](https://doi.org/10.1007/s00338-019-01771-2)

763 Hawkes, L. A., Broderick, A. C., Godfrey, M. H., & Godley, B. J. (2007). Investigating the
 764 potential impacts of climate change on a marine turtle population. *Global Change Biology*,
 765 13(5), 923–932. <https://doi.org/10.1111/j.1365-2486.2007.01320.x>

766 Hénin, C., & Cresswell, G. R. (2005). Upwelling along the western barrier reef of New
 767 Caledonia. *Marine and Freshwater Research*, 56(7), 1005.
 768 <https://doi.org/10.1071/MF04266>

769 Hoegh-Guldberg, O., Cai, R., Poloczanska, E., Brewer, P., Sundby, S., Helmi, K., et al. (2014).
 770 The Ocean. In V. Barros, C. Field, D. Dokken, M. Mastrandrea, K. Mach, T. Bilir, et al.
 771 (Eds.), *Climate Change 2014: Impacts, Adaptation, and Vulnerability. Contribution of*
 772 *Working Group 2 to the Fifth Assessment Report of the Intergovernmental Panel on Climate*
 773 *Change*. Cambridge, United Kingdom and New York, NY, USA: Cambridge University
 774 Press.

775 Hume, B. C. C., Mejia-Restrepo, A., Voolstra, C. R., & Berumen, M. L. (2020). Fine-scale
 776 delineation of Symbiodiniaceae genotypes on a previously bleached central Red Sea reef
 777 system demonstrates a prevalence of coral host-specific associations. *Coral Reefs*, 1–19.
 778 <https://doi.org/10.1007/s00338-020-01917-7>

779 Jiang, H., Farrar, J. T., Beardsley, R. C., Chen, R., & Chen, C. (2009). Zonal surface wind jets
 780 across the Red Sea due to mountain gap forcing along both sides of the Red Sea.
 781 *Geophysical Research Letters*, 36(19), L19605. <https://doi.org/10.1029/2009GL040008>

782 Joseph, P. V., Eischeid, J. K., Pyle, R. J., Joseph, P. V., Eischeid, J. K., & Pyle, R. J. (1994).
 783 Interannual variability of the onset of the Indian Summer Monsoon and its association with
 784 atmospheric features, El Niño, and sea surface temperature anomalies. *Journal of Climate*.
 785 [https://doi.org/10.1175/1520-0442\(1994\)007<0081:IVOTOO>2.0.CO;2](https://doi.org/10.1175/1520-0442(1994)007<0081:IVOTOO>2.0.CO;2)

786 Kakatkar, R., Gnanaseelan, C., Chowdary, J. S., Parekh, A., & Deepa, J. S. (2018). Indian
 787 summer monsoon rainfall variability during 2014 and 2015 and associated Indo-Pacific
 788 upper ocean temperature patterns. *Theoretical and Applied Climatology*, 131(3–4), 1235–

789 1247. <https://doi.org/10.1007/s00704-017-2046-4>

790 Karnauskas, K. B. (2020). Physical diagnosis of the 2016 Great Barrier Reef bleaching event.

791 *Geophysical Research Letters*. <https://doi.org/10.1029/2019GL086177>

792 Karnauskas, K. B., & Cohen, A. L. (2012). Equatorial refuge amid tropical warming. *Nature*

793 *Climate Change*, 2, 530–534. <https://doi.org/10.1038/nclimate1499>

794 Kleypas, J. A., & Burrage, D. M. (1994). Satellite observations of circulation in the southern

795 Great Barrier Reef, Australia. *International Journal of Remote Sensing*, 15(10), 2051–2063.

796 <https://doi.org/10.1080/01431169408954227>

797 Kuo, N. J., Zheng, Q., & Ho, C. R. (2000). Satellite observation of upwelling along the western

798 coast of the South China Sea. *Remote Sensing of Environment*, 74(3), 463–470.

799 [https://doi.org/10.1016/S0034-4257\(00\)00138-3](https://doi.org/10.1016/S0034-4257(00)00138-3)

800 Laloë, J.-O., Cozens, J., Renom, B., Taxonera, A., & Hays, G. C. (2014). Effects of rising

801 temperature on the viability of an important sea turtle rookery. *Nature Climate Change*,

802 4(6), 513–518. <https://doi.org/10.1038/nclimate2236>

803 Laloë, J.-O., Esteban, N., Berkel, J., & Hays, G. C. (2016). Sand temperatures for nesting sea

804 turtles in the Caribbean: Implications for hatchling sex ratios in the face of climate change.

805 *Journal of Experimental Marine Biology and Ecology*, 474, 92–99.

806 <https://doi.org/10.1016/j.jembe.2015.09.015>

807 Laloë, J.-O., Cozens, J., Renom, B., Taxonera, A., & Hays, G. C. (2017). Climate change and

808 temperature-linked hatchling mortality at a globally important sea turtle nesting site. *Global*

809 *Change Biology*, 23(11), 4922–4931. <https://doi.org/10.1111/gcb.13765>

810 Leichter, J., Stewart, H. L., & Miller, S. L. (2003). Episodic nutrient transport to Florida coral

811 reefs. *Limnology and Oceanography*, 48(4), 1394–1407.

812 <https://doi.org/10.4319/lo.2003.48.4.1394>

813 Leichter, J., Deane, G. B., & Stokes, M. D. (2005). Spatial and temporal variability of internal
814 wave forcing on a coral reef. *Journal of Physical Oceanography*, 35(11), 1945–1962.

815 Lentz, S. J., Churchill, J. H., Marquette, C., & Smith, J. (2013). Evaluation and recommendations
816 for improving the accuracy of an inexpensive water temperature logger. *Journal of*
817 *Atmospheric and Oceanic Technology*, 30(7), 1576–1582. <https://doi.org/10.1175/JTECH->
818 D-12-00204.1

819 Liu, G., Strong, A. E., & Skirving, W. (2003). Remote sensing of sea surface temperatures
820 during 2002 Barrier Reef coral bleaching. *Eos, Transactions American Geophysical Union*,
821 84(15), 137–141. <https://doi.org/10.1029/2003EO150001>

822 Liu, G., Heron, S., Eakin, C., Muller-Karger, F., Vega-Rodriguez, M., Guild, L., et al. (2014).
823 Reef-scale thermal stress monitoring of coral ecosystems: new 5-km global products from
824 NOAA Coral Reef Watch. *Remote Sensing*, 6(11), 11579–11606.
825 <https://doi.org/10.3390/rs61111579>

826 Mancini, A., Elsadek, I., & El-Alwany, M. A. N. (2015). Marine turtles of the Red Sea. In N.
827 Rasul & I. Stewart (Eds.), *The Red Sea* (pp. 551–565). Springer, Berlin, Heidelberg.
828 https://doi.org/10.1007/978-3-662-45201-1_31

829 Manzello, D. P., Kleypas, J. A., Budd, D. A., Eakin, C. M., Glynn, P. W., & Langdon, C. (2008).
830 Poorly cemented coral reefs of the eastern tropical Pacific: Possible insights into reef
831 development in a high-CO₂ world. *Proceedings of the National Academy of Sciences*,
832 105(30), 10450.

833 Mishra, V., Aadhar, S., Asoka, A., Pai, S., & Kumar, R. (2016). On the frequency of the 2015
834 monsoon season drought in the Indo-Gangetic Plain. *Geophysical Research Letters*, 43(23),

835 12,102–12,112. <https://doi.org/10.1002/2016GL071407>

836 Mrosovsky, N. (1994). Sex ratios of Sea Turtles. *The Journal of Experimental Zoology*, 270, 16–

837 27. <https://doi.org/10.1002/jez.1402700104>

838 Nadaoka, K., Nihei, Y., Kumano, R., Yokobori, T., Omija, T., & Wakaki, K. (2001). A field

839 observation on hydrodynamic and thermal environments of a fringing reef at Ishigaki Island

840 under typhoon and normal atmospheric conditions. *Coral Reefs*, 20(4), 387–398.

841 <https://doi.org/10.1007/s00338-001-0188-3>

842 NASA Goddard Space Flight Center, Ocean Ecology Lab, O. B. P. G. (n.d.-a). *Moderate-*

843 *resolution Imaging Spectroradiometer (MODIS) Aqua SST Data*. Accessed 02/01/2010.

844 Greenbelt, MD, USA.

845 NASA Goddard Space Flight Center, Ocean Ecology Lab, O. B. P. G. (n.d.-b). *Moderate-*

846 *resolution Imaging Spectroradiometer (MODIS) Terra SST Data*. Accessed 02/01/2010.

847 Greenbelt, MD, USA.

848 Nykjaer, L., & Van Camp, L. (1994). Seasonal and interannual variability of coastal upwelling

849 along northwest Africa and Portugal from 1981 to 1991. *Journal of Geophysical Research*,

850 99(C7), 14197–14207. <https://doi.org/10.1029/94jc00814>

851 Osman, E. O., Smith, D. J., Ziegler, M., Kürten, B., Conrad, C., El-Haddad, K. M., et al. (2018).

852 Thermal refugia against coral bleaching throughout the northern Red Sea. *Global Change*

853 *Biology*, 24(2), e474–e484. <https://doi.org/10.1111/gcb.13895>

854 Packard, G. C., Tracy, C. R., & Roth, J. J. (1977). The physiological ecology of reptilian eggs

855 and embryos, and the evolution of viviparity within the class Reptilia. *Biological Reviews*,

856 52(1), 71–105. <https://doi.org/10.1111/j.1469-185X.1977.tb01346.x>

857 Pan, X., Wong, G. T. F., DeCarlo, T. M., Tai, J.-H., & Cohen, A. L. (2017). Validation of the

858 remotely sensed nighttime sea surface temperature in the shallow waters at the Dongsha
859 Atoll. *Terrestrial, Atmospheric and Oceanic Sciences*, 28(3), 517.
860 <https://doi.org/10.3319/TAO.2017.03.30.01>

861 Patzert, W. C. (1974). Wind-induced reversal in Red Sea circulation. *Deep Sea Research and*
862 *Oceanographic Abstracts*, 21(2), 109–121. [https://doi.org/10.1016/0011-7471\(74\)90068-0](https://doi.org/10.1016/0011-7471(74)90068-0)

863 Pearman, J. K., Ellis, J., Irigoien, X., Sarma, Y. V. B., Jones, B. H., & Carvalho, S. (2017).
864 Microbial planktonic communities in the Red Sea: high levels of spatial and temporal
865 variability shaped by nutrient availability and turbulence. *Scientific Reports*, 7(1), 1–15.
866 <https://doi.org/10.1038/s41598-017-06928-z>

867 Racault, M. F., Raitsos, D. E., Berumen, M. L., Brewin, R. J. W., Platt, T., Sathyendranath, S., &
868 Hoteit, I. (2015). Phytoplankton phenology indices in coral reef ecosystems: Application to
869 ocean-color observations in the Red Sea. *Remote Sensing of Environment*, 160, 222–234.
870 <https://doi.org/10.1016/j.rse.2015.01.019>

871 Raitsos, D. E., Yi, X., Platt, T., Racault, M.-F., Brewin, R. J. W., Pradhan, Y., et al. (2015).
872 Monsoon oscillations regulate fertility of the Red Sea. *Geophysical Research Letters*, 42(3),
873 855–862. <https://doi.org/10.1002/2014GL062882>

874 Ralston, D. K., Jiang, H., & Farrar, J. T. (2013). Waves in the Red Sea: Response to monsoonal
875 and mountain gap winds. *Continental Shelf Research*, 65, 1–13.
876 <https://doi.org/10.1016/J.CSR.2013.05.017>

877 Reid, E. C., DeCarlo, T. M., Cohen, A. L., Wong, G. T. F., Lentz, S. J., Safaie, A., et al. (2019).
878 Internal waves influence the thermal and nutrient environment on a shallow coral reef.
879 *Limnology and Oceanography*, 64(5), 1949–1965. <https://doi.org/10.1002/lno.11162>

880 Reynolds, R. W., Smith, T. M., Liu, C., Chelton, D. B., Casey, K. S., & Schlax, M. G. (2007).

881 Daily high-resolution-blended analyses for sea surface temperature. *Journal of Climate*,
882 20(22), 5473–5496. <https://doi.org/10.1175/2007JCLI1824.1>

883 Richards, Z. T., Garcia, R., Moore, G., Fromont, J., Kirkendale, L., Bryce, M., et al. (2019). A
884 tropical Australian refuge for photosymbiotic benthic fauna. *Coral Reefs*, 38, 669–676.
885 <https://doi.org/10.1007/s00338-019-01809-5>

886 Riegl, B., & Piller, W. E. (2003). Possible refugia for reefs in times of environmental stress.
887 *International Journal of Earth Sciences*, 92(4), 520–531. [https://doi.org/10.1007/s00531-](https://doi.org/10.1007/s00531-003-0328-9)
888 003-0328-9

889 Roberts, M. B., Jones, G. P., McCormick, M. I., Munday, P. L., Neale, S., Thorrold, S., et al.
890 (2016). Homogeneity of coral reef communities across 8 degrees of latitude in the Saudi
891 Arabian Red Sea. *Marine Pollution Bulletin*, 105(2), 558–565.
892 <https://doi.org/10.1016/J.MARPOLBUL.2015.11.024>

893 Robitzch, V. S. N., Lozano-Cortés, D., Kandler, N. M., Salas, E., & Berumen, M. L. (2016).
894 Productivity and sea surface temperature are correlated with the pelagic larval duration of
895 damselfishes in the Red Sea. *Marine Pollution Bulletin*, 105(2), 566–574.
896 <https://doi.org/10.1016/j.marpolbul.2015.11.045>

897 Rodríguez, S., & Cróquer, A. (2008). Dynamics of Black Band Disease in a *Diploria strigosa*
898 population subjected to annual upwelling on the northeastern coast of Venezuela. *Coral*
899 *Reefs*, 27(2), 381–388. <https://doi.org/10.1007/s00338-007-0341-8>

900 Safaie, A., Silbiger, N. J., McClanahan, T. R., Pawlak, G., Barshis, D. J., Hench, J. L., et al.
901 (2018). High frequency temperature variability reduces the risk of coral bleaching. *Nature*
902 *Communications*, 9(1), 1671. <https://doi.org/10.1038/s41467-018-04074-2>

903 Schmidt, G. M., Wall, M., Taylor, M., Jantzen, C., & Richter, C. (2016). Large-amplitude

904 internal waves sustain coral health during thermal stress. *Coral Reefs*, 1–13.

905 <https://doi.org/10.1007/s00338-016-1450-z>

906 Smith, N. P. (2001). Weather and hydrographic conditions associated with coral bleaching: Lee
 907 Stocking Island, Bahamas. *Coral Reefs*, 20(4), 415–422. [https://doi.org/10.1007/s00338-](https://doi.org/10.1007/s00338-001-0189-2)
 908 001-0189-2

909 Sofianos, S. S., & Johns, W. E. (2007). Observations of the summer Red Sea circulation. *Journal*
 910 *of Geophysical Research*, 112(C6), C06025. <https://doi.org/10.1029/2006JC003886>

911 Spalding, M. D., Fox, H. E., Allen, G. R., Davidson, N., Ferdaña, Z. A., Finlayson, M., et al.
 912 (2007). Marine Ecoregions of the World: A Bioregionalization of Coastal and Shelf Areas.
 913 *BioScience*, 57(7), 573–583. <https://doi.org/10.1641/b570707>

914 Strong, A. E., Liu, G., Kimura, T., Yamano, H., Tsuchiya, M., Kakuma, S. I., & Van Woesik, R.
 915 (2002). Detecting and monitoring 2001 coral reef bleaching events in Ryukyu Islands, Japan
 916 using satellite bleaching hotspot remote sensing technique. In *International Geoscience and*
 917 *Remote Sensing Symposium (IGARSS)* (Vol. 1, pp. 237–239).
 918 <https://doi.org/10.1109/igarss.2002.1024998>

919 Tang, D. L., Kester, D. R., Ni, I. H., Kawamura, H., & Hong, H. (2002). Upwelling in the
 920 Taiwan Strait during the summer monsoon detected by satellite and shipboard
 921 measurements. *Remote Sensing of Environment*, 83(3), 457–471.
 922 [https://doi.org/10.1016/S0034-4257\(02\)00062-7](https://doi.org/10.1016/S0034-4257(02)00062-7)

923 Taylor, J. G., & Pearce, A. F. (1999). Ningaloo Reef currents: implications for coral spawn
 924 dispersal, zooplankton and whale shark abundance. *Journal of the Royal Society of Western*
 925 *Australia*, 82, 57–65.

926 Viswanadhapalli, Y., Dasari, H. P., Langodan, S., Challa, V. S., & Hoteit, I. (2017). Climatic

927 features of the Red Sea from a regional assimilative model. *International Journal of*
928 *Climatology*, 37(5), 2563–2581. <https://doi.org/10.1002/joc.4865>

929 Wang, Y. H., Dai, C. F., & Chen, Y. Y. (2007). Physical and ecological processes of internal
930 waves on an isolated reef ecosystem in the South China Sea. *Geophysical Research Letters*,
931 34(18), L18609. [https://doi.org/https://doi.org/10.1029/2007GL030658](https://doi.org/10.1029/2007GL030658)

932 Wellington, G. M., Strong, A. E., & Merlen, G. (2001). Sea surface temperature variation in the
933 Galápagos Archipelago: a comparison between AVHRR nighttime satellite data and in situ
934 instrumentation (1982-1998). *Bulletin of Marine Science*, 69, 27–42.

935 Wessel, P., & Smith, W. H. F. (1996). A global, self-consistent, hierarchical, high-resolution
936 shoreline database. *Journal of Geophysical Research: Solid Earth*, 101(B4), 8741–8743.
937 <https://doi.org/10.1029/96jb00104>

938 Wiedenmann, J., D’Angelo, C., Smith, E. G., Hunt, A. N., Legiret, F.-E., Postle, A. D., &
939 Achterberg, E. P. (2013). Nutrient enrichment can increase the susceptibility of reef corals
940 to bleaching. *Nature Climate Change*, 3(2), 160–164.
941 [https://doi.org/https://doi.org/10.1038/nclimate1661](https://doi.org/10.1038/nclimate1661)

942 van Woesik, R. (2004). Comment on “Coral Reef Death During the 1997 Indian Ocean Dipole
943 Linked to Indonesian Wildfires.” *Science*, 303(5662), 1297a – 1297.
944 <https://doi.org/10.1126/science.1091983>

945 Wolanski, E., & Bennett, A. (1983). Continental shelf waves and their influence on the
946 circulation around the Great Barrier Reef. *Marine and Freshwater Research*, 34(1), 23.
947 <https://doi.org/10.1071/MF9830023>

948 Wolanski, E., & Pickard, G. (1983). Upwelling by internal tides and kelvin waves at the
949 continental shelf break on the Great Barrier Reef. *Marine and Freshwater Research*, 34(1),

950 65. <https://doi.org/10.1071/MF9830065>

951 Wyatt, A. S. J., Leichter, J. J., Toth, L. T., Miyajima, T., Aronson, R. B., & Nagata, T. (2019).

952 Heat accumulation on coral reefs mitigated by internal waves. *Nature Geoscience*, *13*, 28–

953 34. <https://doi.org/10.1038/s41561-019-0486-4>

954

955

Figures

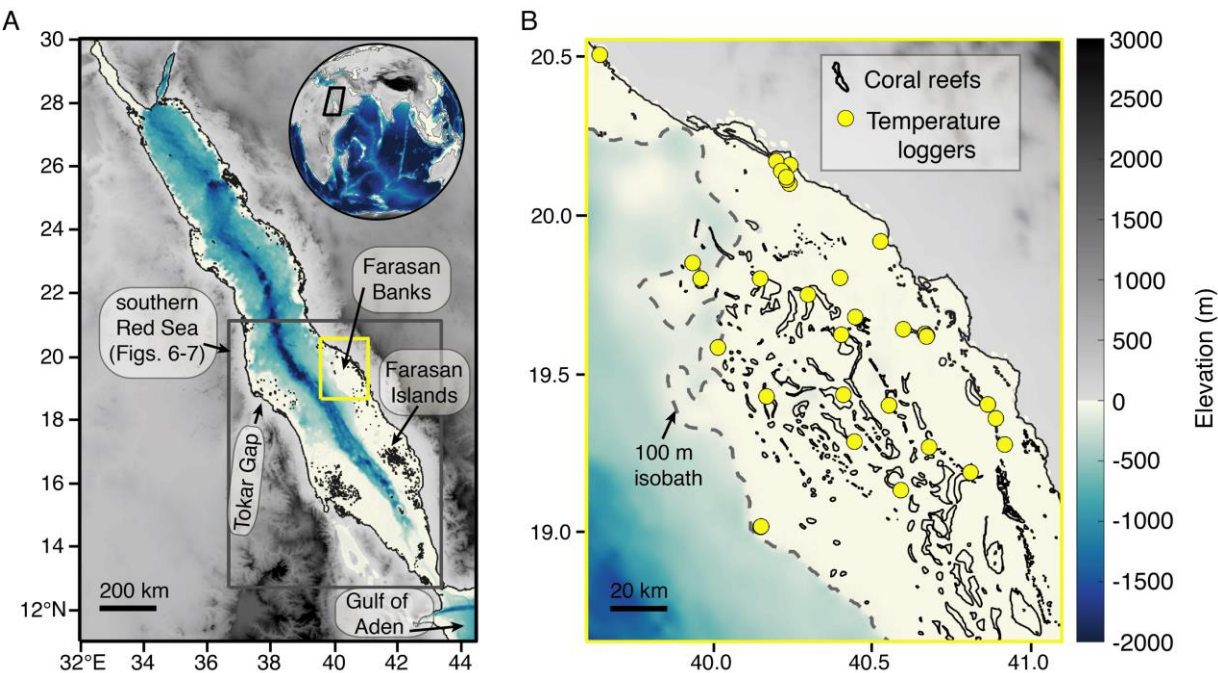


Figure 1. Land topography and ocean bathymetry of the (A) Red Sea and (B) Farasan Banks. In (A), the dark gray box shows the area of the southern Red Sea assessed for wind and sea surface height patterns (shown in Figs. 6-7). The yellow box shows the area of the Farasan Banks shown in panel (B) and in analyses of temperature logger data (Figs. 4, 5, 8). In (B), yellow circles show locations of temperature loggers and black outlines show coral reef locations. Not all temperature loggers were deployed for the entire study period, as described in the text and plotted in Figs. 4-5. The dashed gray line shows the 100-m isobath used to define the shelf edge.

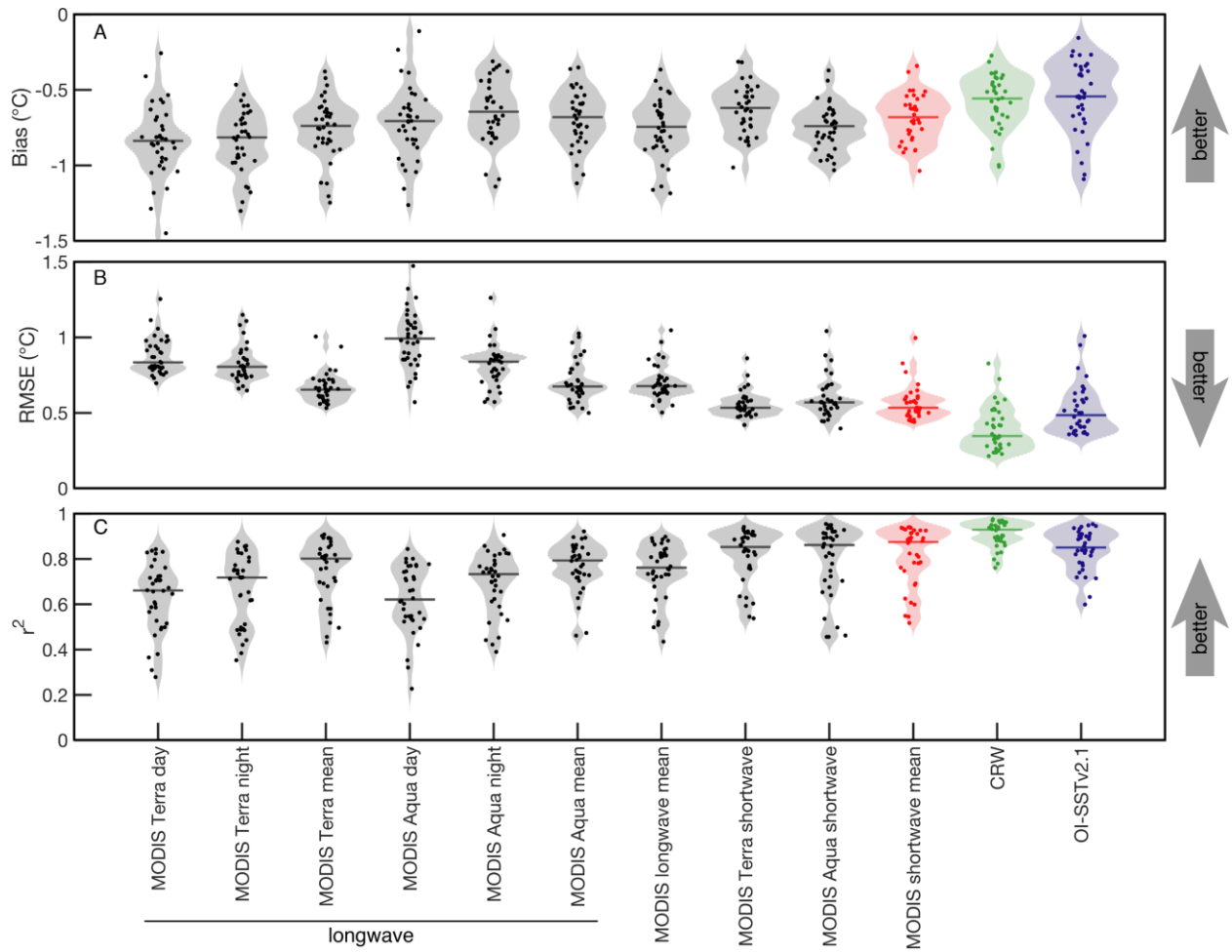


Figure 2. Descriptive statistics of satellite-logger mismatches. (A) Bias shows the overall difference in means, with negative values indicating that satellite-derived SST is lower than logger temperatures. (B) RMSE shows the differences from the 1:1 relationship after accounting for the Bias. (C) Coefficient of determination (r^2) shows the skill of satellites in tracking variations in logger temperatures. The three satellite-SST products used in further analyses are shown in colors (red, MODIS shortwave mean; green, CRW; blue, OI-SSTv2). Circles indicate the values for individual temperature loggers (x-axes positions randomly offset for clarity), the shaded areas show relative distributions, and the horizontal bars show medians.

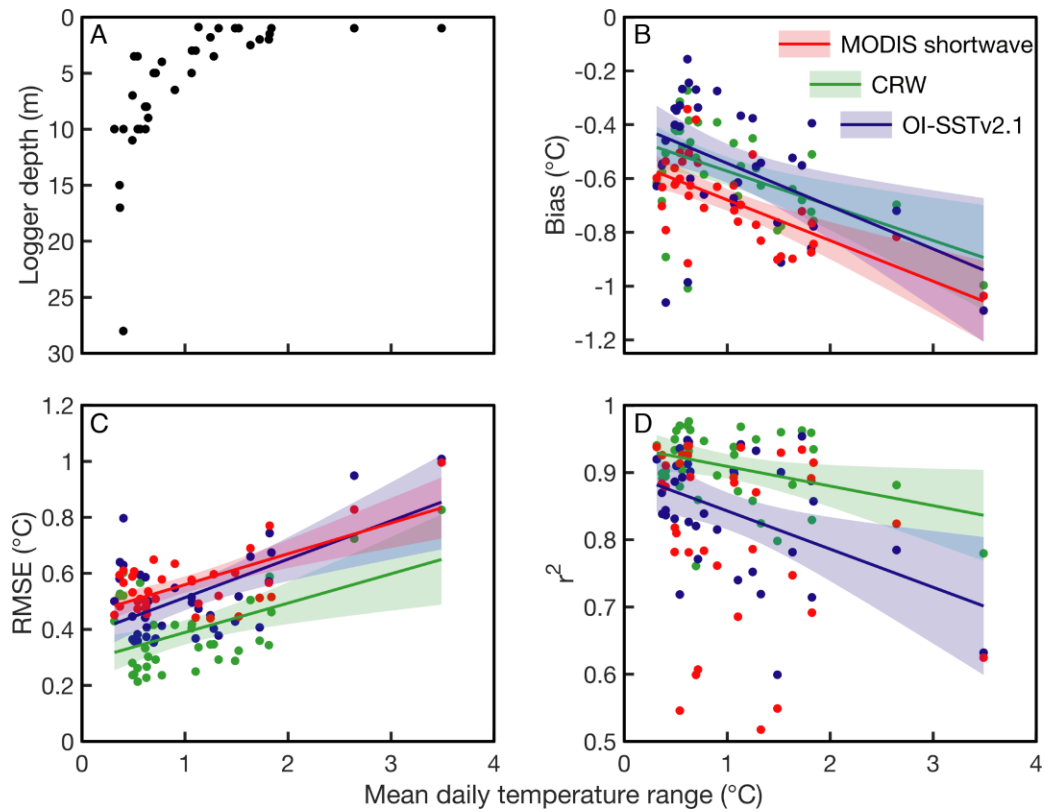


Figure 3. Relationships between depth, daily temperature range, and satellite-logger mismatches. (A) Logger depths versus daily temperature range show that deeper loggers were located in more thermally stable environments. (B-D) Bias, RMSE, and r^2 between satellites and loggers versus daily temperature range. For each statistic, the significant ($p < 0.05$) trends are plotted with shading indicating 95% uncertainty of the regression. Each point represents a single temperature logger.

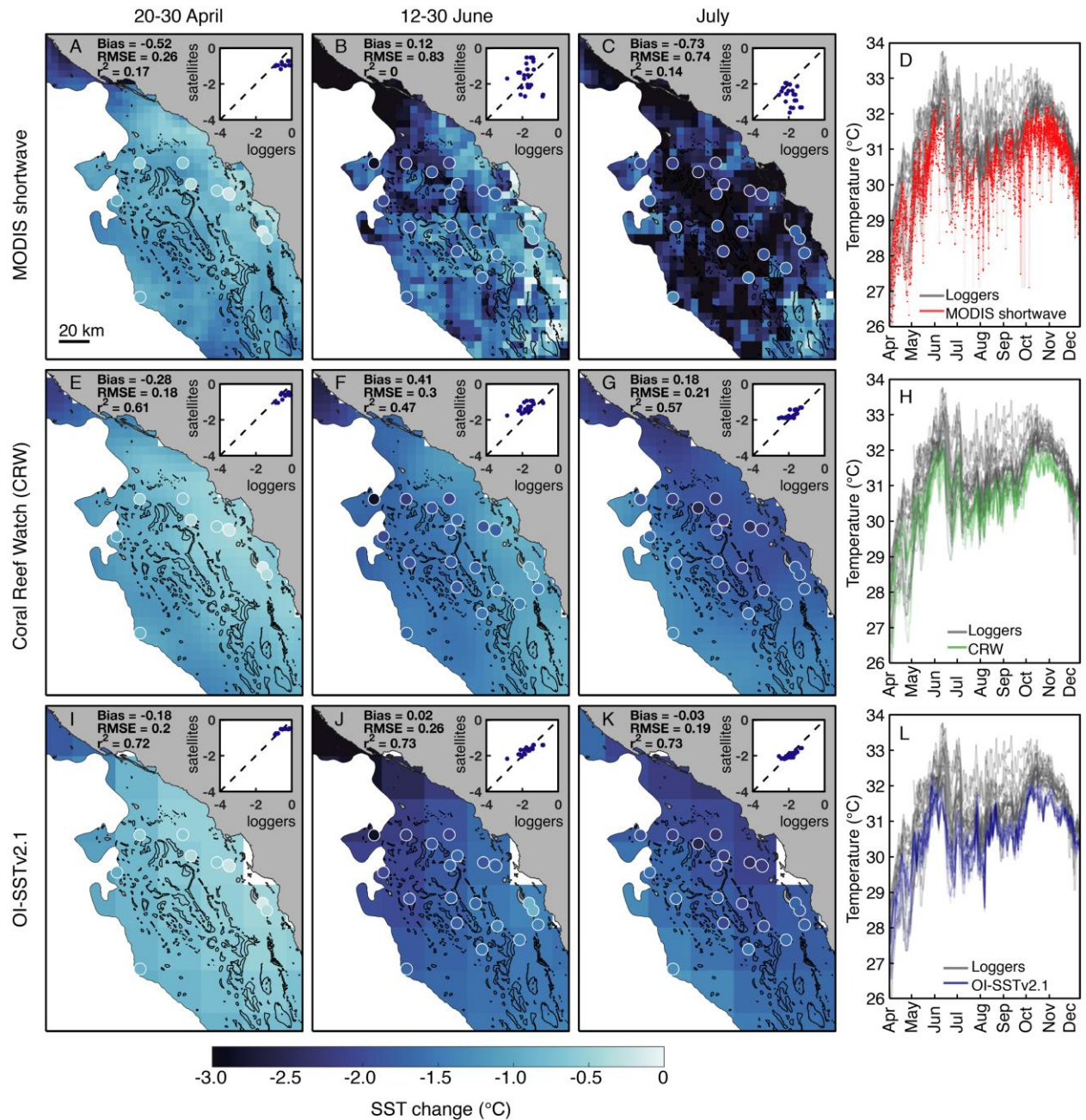


Figure 4. Satellite and logger detection of upwelling in the Farasan Banks during 2019. In map panels, colors show the change in temperature due to upwelling, calculated as the difference between minimum and maximum temperature across different time ranges (see text for details). Satellite-based upwelling is shown as the colored grid-boxes, which are overlaid by upwelling detected in temperature loggers (circles with white outer ring). Land is shown in gray, and off-

shelf deep waters are shown in white. Correlation plots in upper right of each map shows the satellite- and logger-based intensities of upwelling, compared on a point-by-point basis. The descriptive statistics (Bias, RMSE, r^2) for each panel are shown toward the upper left. Different time periods are shown in columns (April: A,E,I; June: B,F,J; July: C,G,K), and different satellite products are shown in rows (MODIS shortwave: A-D, CRW: E-H, OI-SSTv2: I-L). Time series panels (D,H,L) show the temperature from *in situ* loggers (gray) and each satellite for its grid-boxes covering each temperature loggers (colors). The area shown in each map is indicated in Fig. 1.

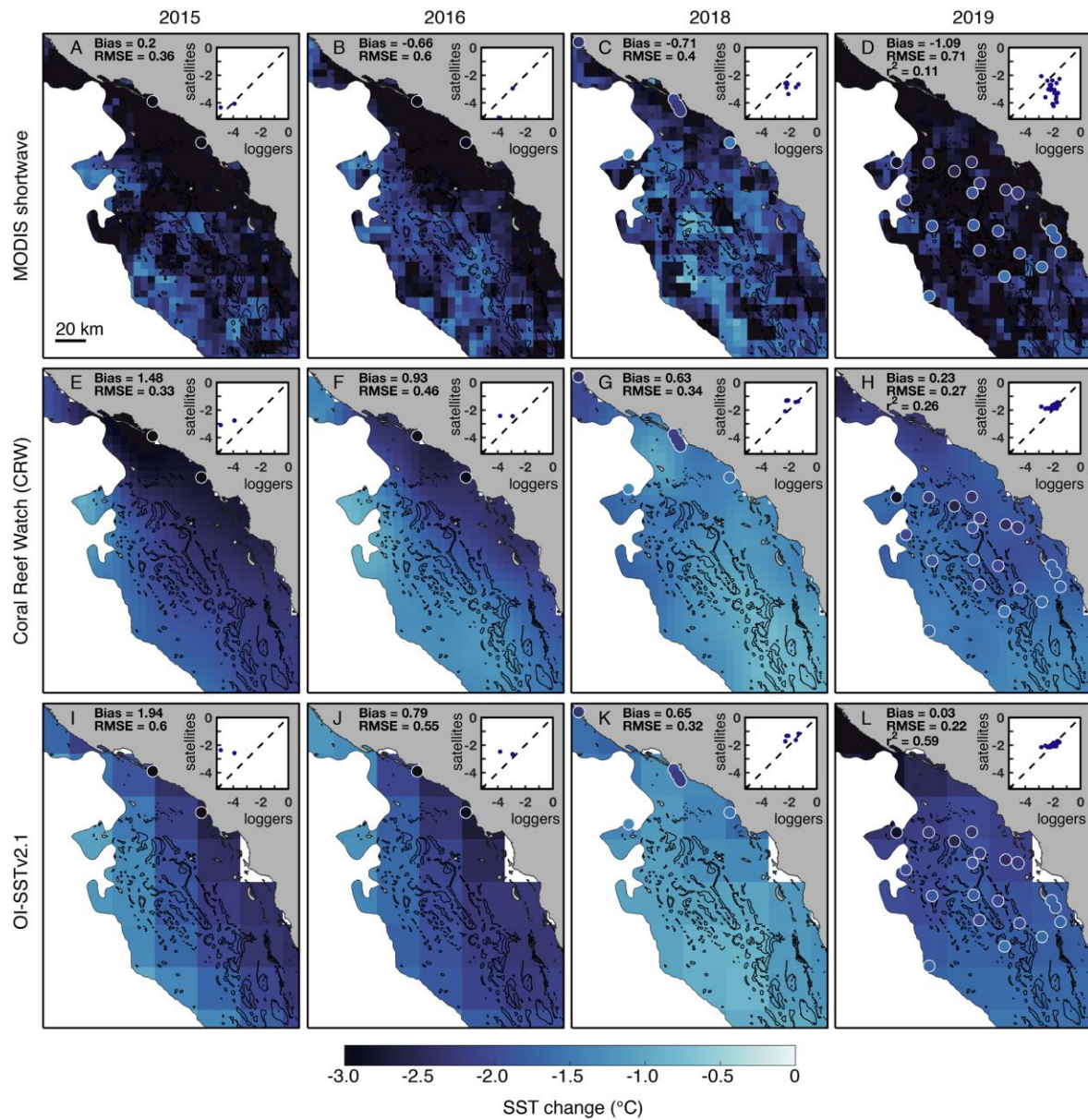


Figure 5. Satellite and logger detection of upwelling in the Farasan Banks during 2015, 2016, 2018, and 2019. The same analyses are shown as in Fig. 4, except only the maximum upwelling intensity per year between the June maximum and July/August minimum is shown. The r^2 is not displayed for pre-2019 years due to the relatively low number of temperature loggers. The year 2017 is missing because temperature loggers were not deployed during June and July. Note that the color range only covers -3 to 0 °C because this captures the full range of upwelling intensity

1010 recorded by CRW and OI-SSTv2.1, but MODIS and the loggers recorded greater cooling (see
1011 cross-plots in upper right of each panel).

1012

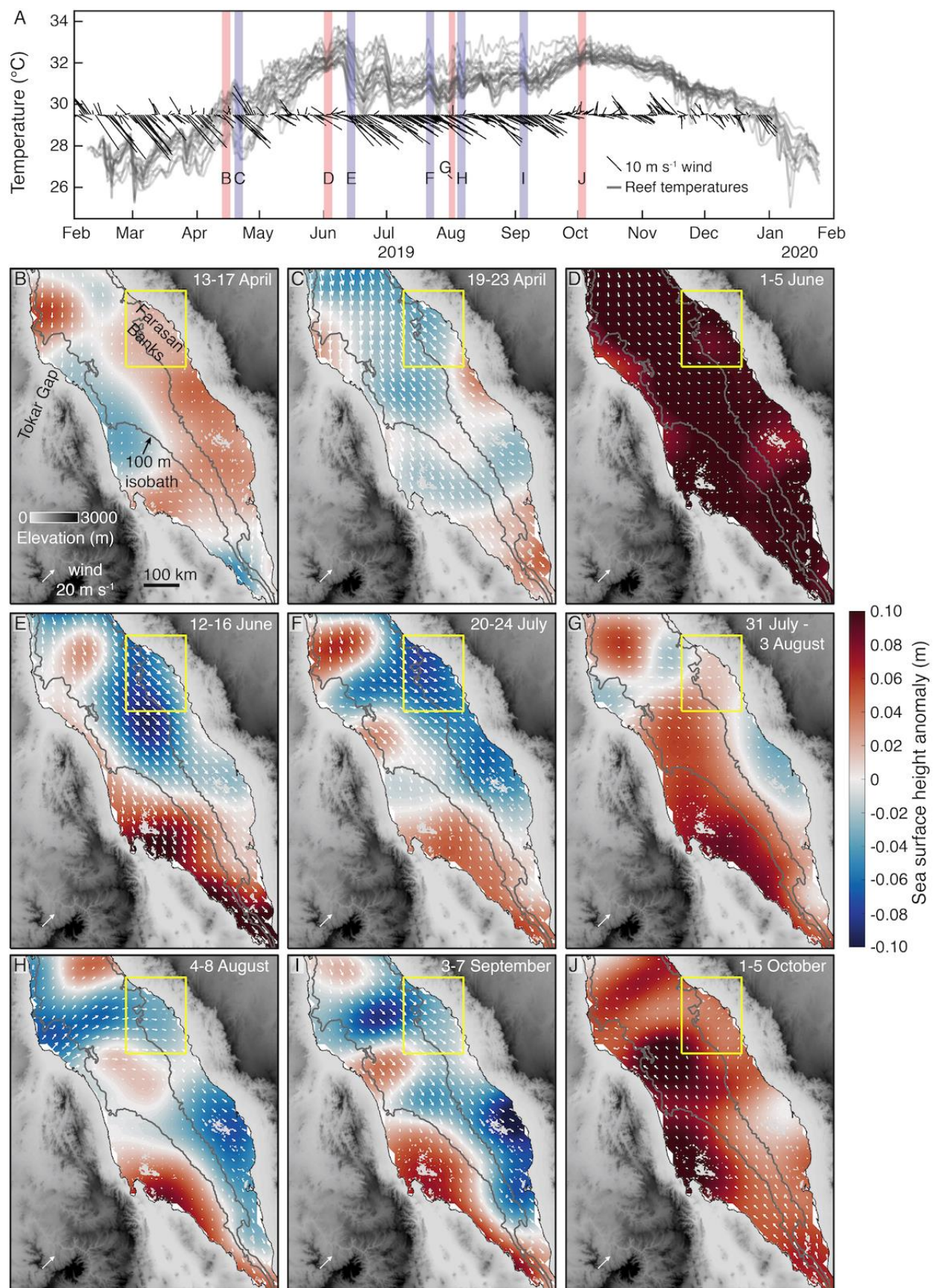


Figure 6. Temporal and spatial relationships between upwelling, winds, and sea surface height (SSH) during 2019. (A) Time series of all Farasan Banks temperature loggers during 2019 (gray) and wind vectors (black), which show both wind speed and direction (the direction the wind is blowing towards, such that vectors pointing to the lower right indicate southeast-ward winds). Vertical bars indicate time periods shown in the map panels (B-J), with relatively high SSH times shown in red and low SSH times shown in blue. (B-J) Maps of wind vectors (white arrows) and SSH anomalies (colors). The gray line shows the 100-m isobath and the grayscale shading shows land topography. The yellow box indicates the Farasan Banks area displayed in other figures.

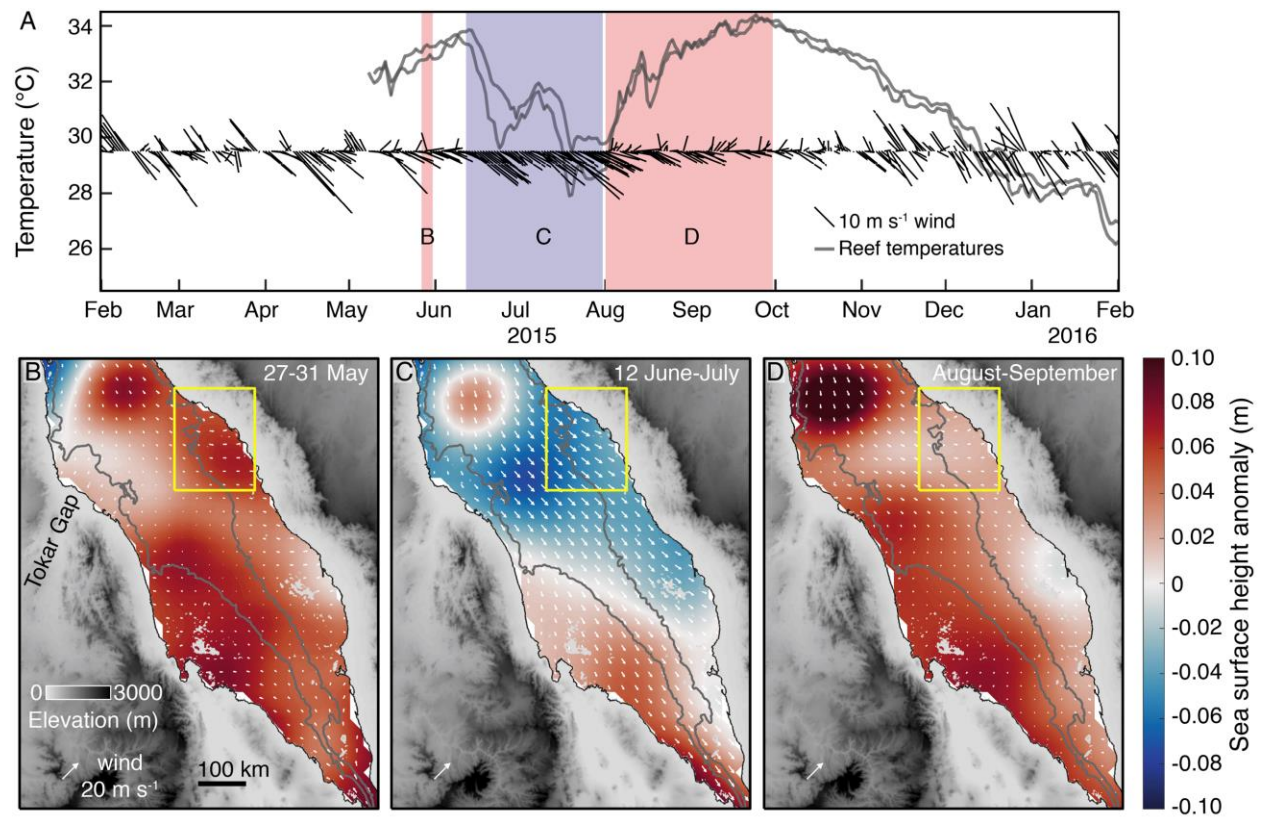


Figure 7. Temporal and spatial relationships between upwelling, winds, and sea surface height (SSH) during 2015. The panels are the same as in Fig. 6, except fewer time periods are displayed.

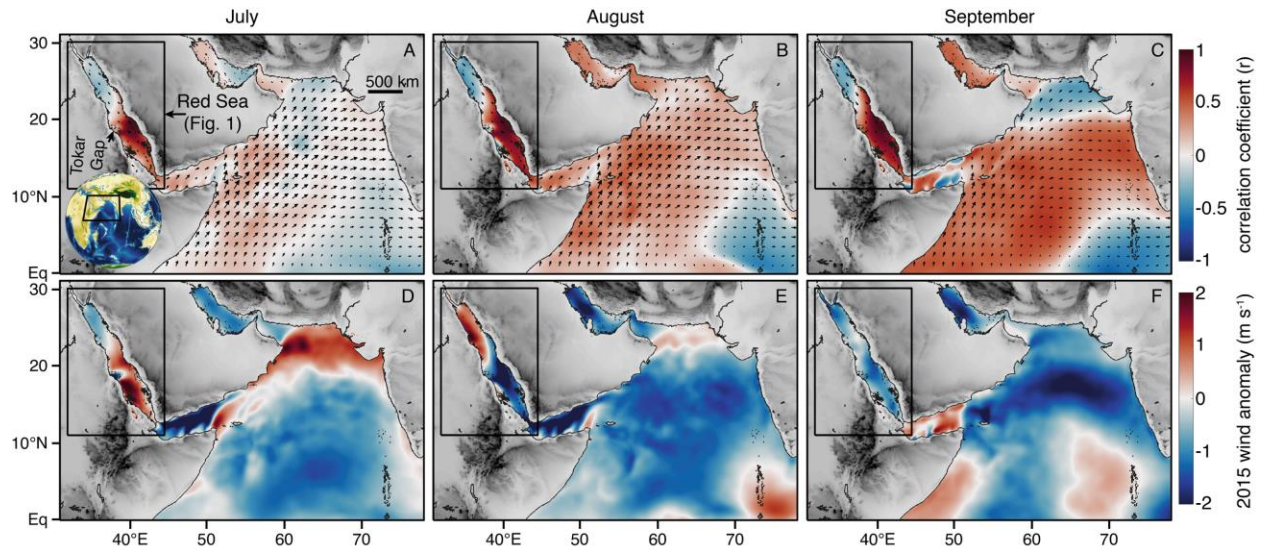


Figure 8. Connection between the Red Sea and southwest Indian monsoons. (A-C) Correlation maps between Farasan Banks and Arabian Sea surface wind anomalies in (A) July, (B) August, and (C) September over the period 1979-2019. Black vectors show the climatological (1982-2012) mean winds during each month. (D-F) Wind anomalies relative to the climatological mean during each month of 2015. Gray box shows the Red Sea area displayed in Fig. 1.

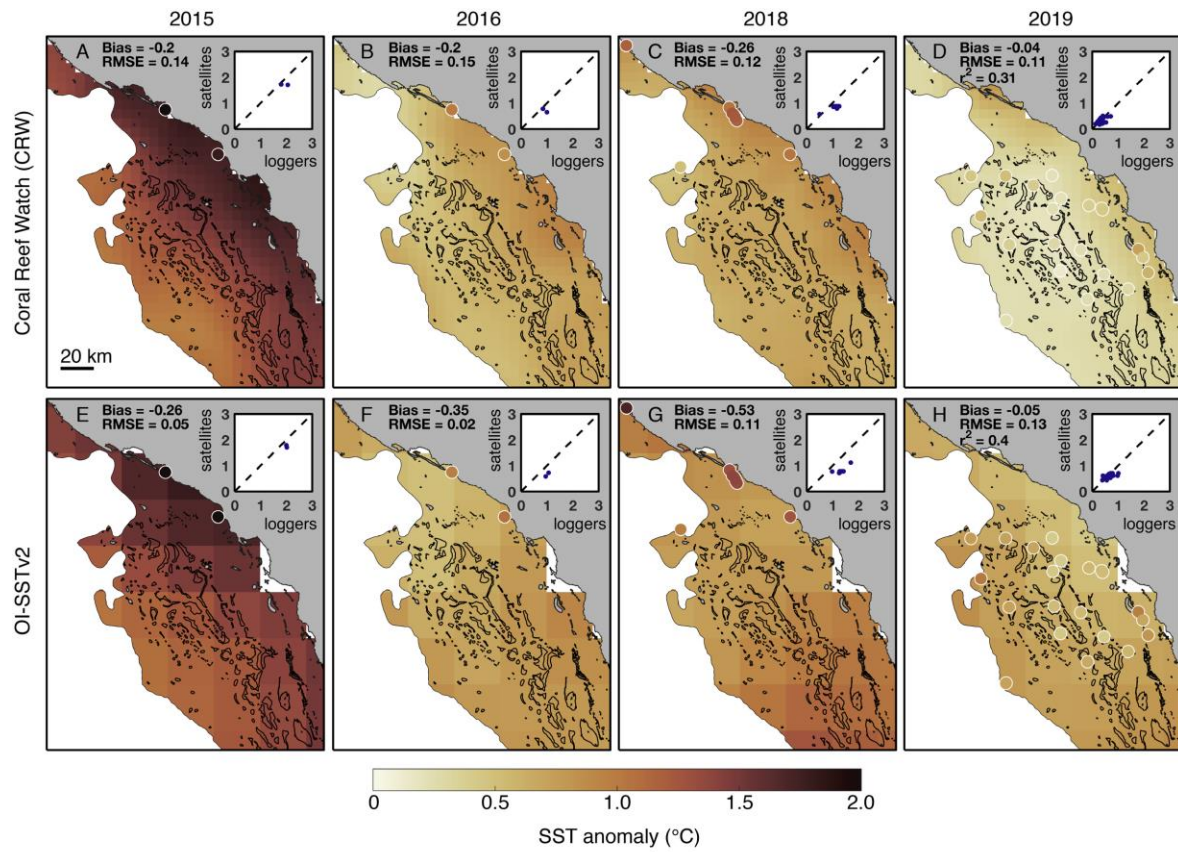


Figure 9. Satellite and logger detection of heat stress in the Farasan Banks during 2015, 2016, 2018, and 2019. The panels are the same as Fig. 5, except that colors show September-October SST maximum anomalies above the maximum monthly mean (MMM).

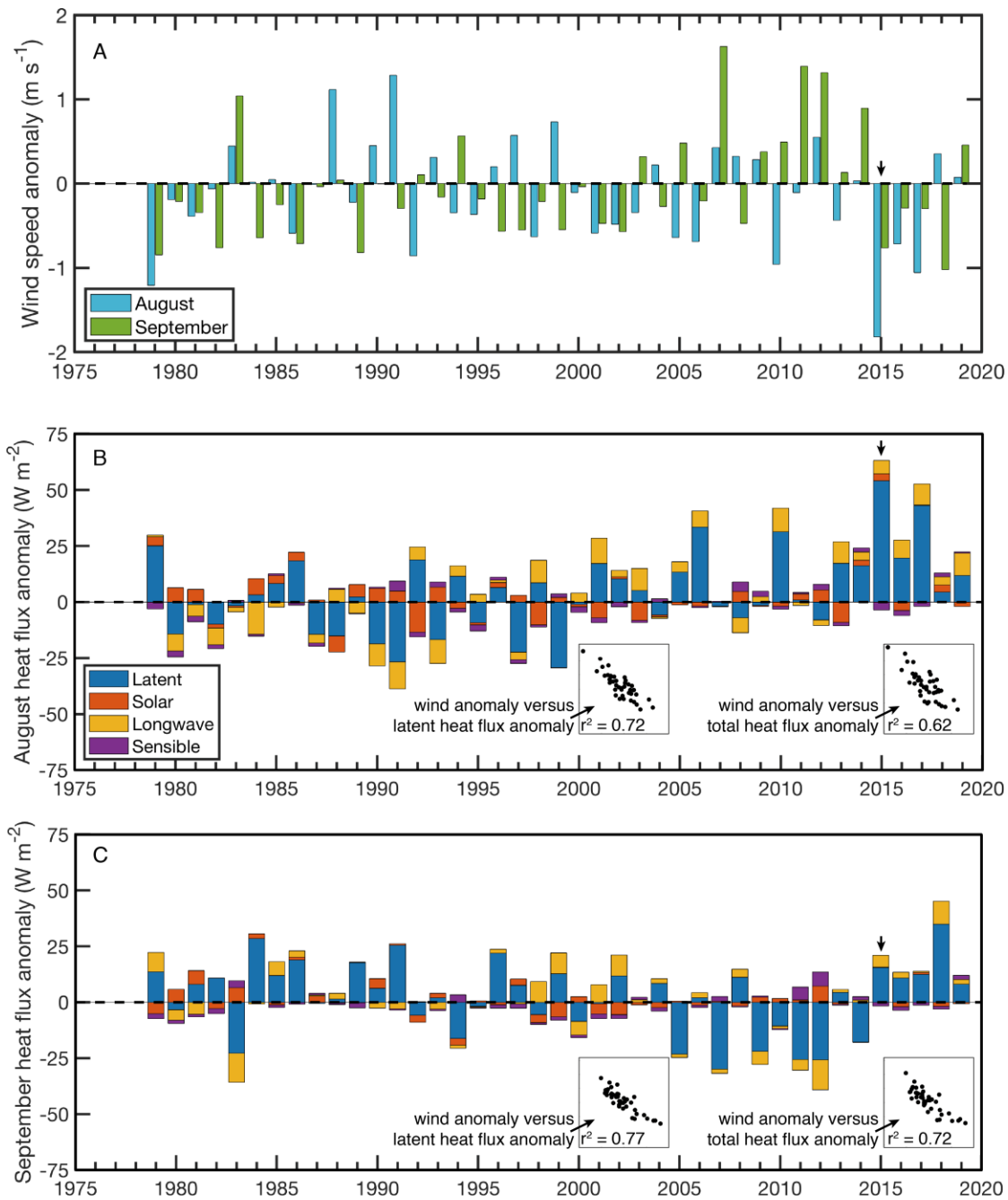


Figure 10. Wind and heat flux anomalies during August and September in the Farasan Banks from 1979 to 2019. (A) Wind speed anomalies during August (light blue) and September (green). (B) Latent (blue), solar (red), longwave (yellow), and sensible (purple) heat flux anomalies during August. The inset boxes show the correlations between the August wind speed anomalies

1053 and the total (sum of all components) and latent heat flux anomalies, where each point represents
1054 one year. (C) Same as panel (B), except for September. The black arrows indicate the year 2015.

1055

1056

1057

1058

1059

1060

1061

1062

1063

1064

1065

1066

1067

1068

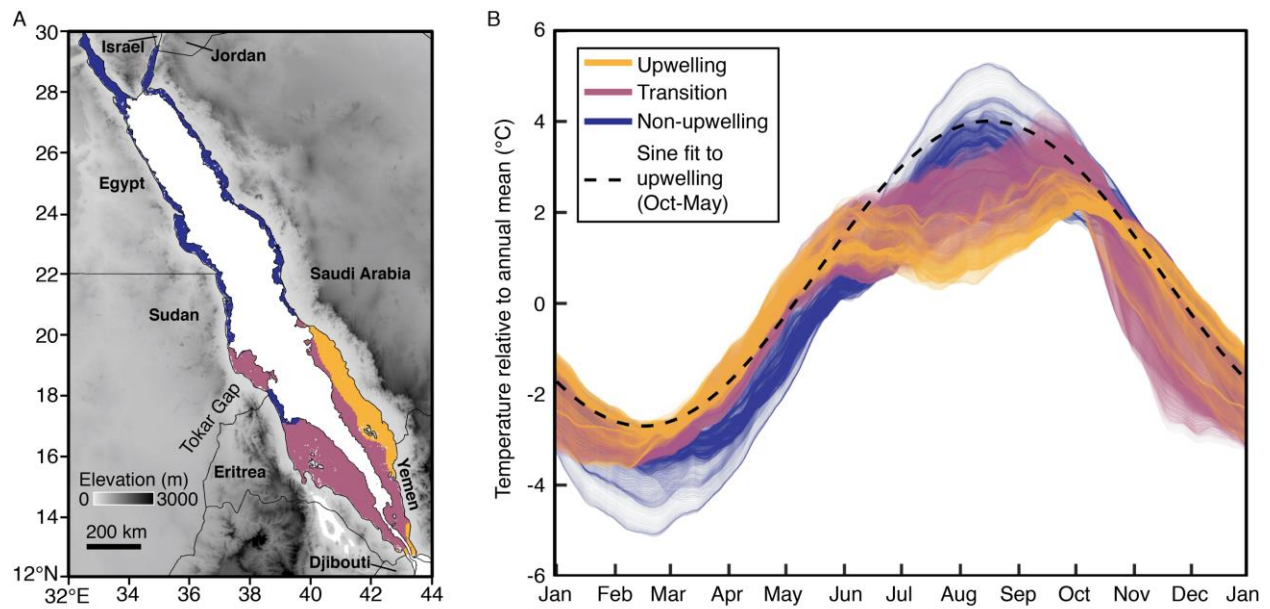


Figure 11. Upwelling zonation in the Red Sea. (A) Map showing the three zones defined here in colors. (B) Seasonal SST cycles (with the mean annual SST removed) for the three zones: upwelling (orange), non-upwelling (blue), and transition (pink). The black dashed line shows a sinusoidal fit to the upwelling zone data from October to May (*i.e.*, excluding June-September), which indicates approximately how much warmer peak temperatures would be in this zone in the absence of upwelling. The map is defined using data from Coral Reef Watch (CRW), with each 5-km pixel's time series plotted in the time series. See the text for details of the definitions of each zone.

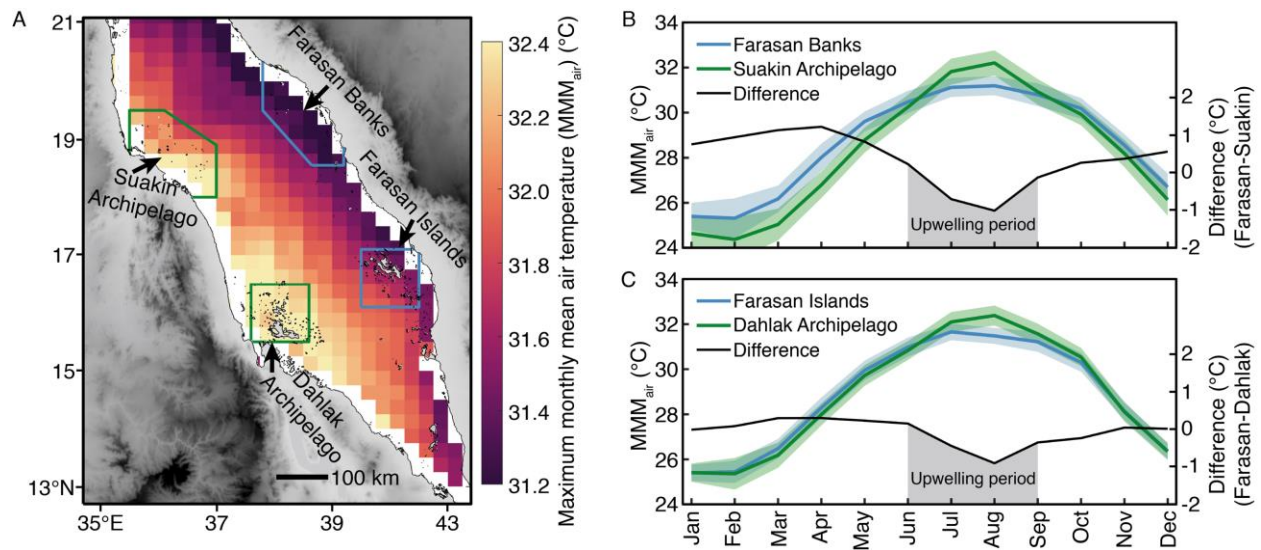


Figure 12. Climatological (1982-2012) seasonal cycles of air temperature (2-m altitude) in the southern Red Sea. (A) map of maximum monthly mean air temperature. (B-C) Seasonal patterns of air temperature in the Farasan Banks and Farasan Islands (light blue, eastern Red Sea) compared to the Suakin and Dahlak Archipelagos (green, western Red Sea). The boxes bounding the sites shown in time series are displayed on the map in (A). The shaded error bounds in (B-C) indicate one standard deviation of the climatology.